SMTA

Journal of Surface Mount Technology

Volume 37, Issue 1, 2024

Journal of Surface Mount Technology
April 2024 | Volume 37, Issue 1
ISSN: 1093-7358

6600 City W Parkway, Suite 300
Eden Prairie, MN 55344, USA

Phone: +1 952-920-7682
journal@smta.org
www.smta.org

COMMITTEE MISSION STATEMENT

The mission of the SMTA Journal Committee is to select and review papers for publication in the Journal of SMT, ensuring a high standard of quality for each issue and ensuring article content best serves SMTA membership.

A very warm greeting from the editorial desk before the summer heats up, especially where I am in Arizona. For starters, I would like to express my heartfelt gratitude and thanks to Brian Roggeman as we bid adieu to him and his services as a Journal reviewer. Congrats to Brian on his promotion, which unfortunately for the Journal comes with added responsibilities and thus prompting him to leave the Journal committee. Brian was a terrific reviewer with his rigor and technical depth, and I personally will miss his expertise in the areas of reliability and testing. Thank you, Brian, and we have a spot open when you are ready to come back.

In this edition we open with a compilation paper that lays out the various criteria used in solder alloy adoption. The second paper tests conformal coating in various testing environments. The last paper investigates solder joint reliability in conjunction with matte-Sn electroplating.

As always, this Journal is dependent on excellent publications submitted by our members. To keep up the high technical standards please consider sending original papers for review to Ryan Flaherty (ryan@smta.org). Remember, the only charge associated with publication is your hard work and intellect unlike several other journals that levy a per page fee.

Lastly, please don't forget to submit an abstract for the 2024 SMTA International Conference & Exposition to be held in Rosemont, IL from October 21 to 24, and make sure to register on time to attend in person.

— *Srini Chada, Ph.D.*
The Journal of SMT Editor/Journal Committee Chair

SUBMIT ORIGINAL PAPERS FOR REVIEW:

1. Go to **https://journal.smta.org** and click "Register"

2. Complete the form to create your profile in the system

3. Once your profile is active, click "Make a Submission"

4. Read all requirements and begin the 5-step process:
   a. Acknowledge and accept the requirements
   b. Upload your paper
   c. Enter metadata
   d. Confirm your submission
   e. Review next steps of the process

Contact Ryan Flaherty with questions: ryan@smta.org

ABOUT THE JOURNAL OF SMT

The Journal of SMT is a quarterly, peer-reviewed, technical publication of articles related to electronic assembly technologies, including microsystems, emerging technologies, and related business operations.

Criteria for Solder Alloy Adoption

Deng Yun Chen[1], Michael Osterman[1], Carol Handwerker[2], Sa'd Hamasha[3]

[1]*University of Maryland*
College Park, MD, USA

[2]*Purdue University*
West Lafayette, IN, USA

[3]*Auburn University*
Auburn, AL

ABSTRACT

Solder is a critical component in modern electronic systems – past, present, and future. While solder is used within packaged electrical devices, the highest volume of solder is used for fabrication of printed circuit board assemblies. Historically, tin-lead solder was the dominant solder used in printed circuit board assemblies. However, tin-silver-copper solder replaced tin-lead solder starting in 2006 after European Union regulations banned the use of lead for a wide range of electronic products. Despite the successful transition to tin-silver-copper lead-free solder and over fifteen years of high volume lead-free electronic production, a number of aerospace and defense products have not converted to tin-silver-copper or other lead-free solders over reliability concerns. Reliability should be a concern for all product manufacturers and end-users. This begs the question, what has convinced industries that are currently producing lead-free products that the reliability was sufficient and what is keeping defense and aerospace electronic equipment manufacturers from adopting lead-free solder. This paper reviews decision processes for adopting solder for printed circuit board assembly.

Key words: ROHS, Solder, Assembly, Reliability, Fatigue.

INTRODUCTION

In 2002, the European Union introduced the Restriction of Hazardous Substance (RoHS) directive that called for the elimination of six hazardous substances found in specific categories of electrical and electronic equipment for product introduced into the European Union marketplace after July 2006 [1]. The leadup to this directive and the issuance of the directive started the clock for electronics manufacturers to find an alternative to the eutectic tin-lead solder alloy that had been used.

Solder provides electrical, thermal, and mechanical connections between electronic components and printed circuit boards. Eutectic tin-lead alloy has been the preferred solder material due to its melting temperature, resistance to tin whisker formation, and reliability under mechanical, thermal, and electrical loads. The restriction of lead use prohibited the majority use of tin-lead solders in commercial electronics and limited the lead-containing components.

In efforts of finding a replacement for tin-lead solder in the early 2000s, near eutectic tin-silver-copper alloys (SAC405, SAC396, and SAC387) were examined. Through a continuing study of the effects of silver concentration in near eutectic SAC alloys, SAC305 alloy became the preferred lead-free solder replacement for SnPb. While the temperature cycling performance of SAC305 and these other higher silver SAC solders are generally superior to SnPb, their drop performance was identified as an issue. In the late 2000s, the popularity of portable electronics further increased attention on SAC305 performance under mechanical loads, primarily vibration and drop/shock. Tin rich lead-free solders with lower silver contents such as SAC105, SAC205, SAC0307, and SN100C were studied [2]. It was found that reducing silver content in SAC improved the drop performance, although the temperature cycling reliability is compromised slightly [3].

Since then, solder alloy research has focused on: 1) solders with high reliability for aerospace, defense, medical, and automobile industries, and (2) solders that have low melting temperatures in the range 130°C to 200°C, well below SAC solder melting temperature, and meet the reliability requirements for commercial microelectronics. For the most demanding applications, design of high performance solders has focused on making SAC solders stronger and more creep resistant by microalloying of bismuth, antimony, nickel, and indium to fulfill the need for higher

temperature cycling and improved mechanical reliability [4][5]. The goal of low melting temperature solders (LTS) is to reduce the reflow temperature by lowering the melting temperature of the solder alloy, and thus to reduce warpage-induced defects while also meeting the reliability requirement for commercial microelectronics. Research has been focusing on near eutectic bismuth-tin (Bi-Sn) alloys and Bi-Sn with alloying additions, which all have melting temperatures near 139°C [6][7].

Although many lead-free alloys are available commercially, commercial microelectronic industries adopted SAC305 as the international standard solder about 15 years ago. As a result, SAC305 has been the most studied, widely accepted, and widely used lead-free solder in global microelectronics. Defense and aerospace industries are still hesitant to switch to lead-free solder. Not all the industries had to go to Pb-free at once, according to RoHS. The question is what persuaded the commercial industries to adopt SAC305 and what factors contributed to the SAC305 adoption. This paper examines the adoption for SAC305 and factors in adopting the next solder alloy.

With Packaged Electronic Devices

Any solder that is selected for printed circuit board assembly must be compatible with terminal finish and terminal base material to which the solder is expected to bond. Currently, copper or copper alloys make up the bulk of base materials for terminations of lead-framed based packaged electronic devices. Other terminal base materials include iron-nickel and nickel. For many array parts, such as ball-grid array parts (BGA), terminations are formed with solder spheres on the component side with SAC305 being the most prevalent solder used for solder spheres. When parts with solder spheres are assembled, paste is used on the board-side. Thus, if the solder paste and the solder sphere are of different alloys, compatibility becomes an issue, and the mixing ratio in heterogeneous solder plays an important role in solder joint quality.

As is widely known, SAC305 is not a "drop-in" replacement for Sn-Pb eutectic solder. One of the dominant factors is the reflow temperature. The melting temperature of SnPb is 183°C while the melting temperature of SAC305 is 217°C. The increase in melting temperature of solder requires higher reflow temperature during assembly, increasing from approximately 220°C to 250°C. For SnPb based assemblies, a thin layer of SnPb (known as a "surface finish") is electroplated on Cu pads on printed circuit boards to protect the Cu surfaces from environmental contamination and maintain solderability. With the ban on the use of Pb, lead-free assemblies require alternative surface finishes to SnPb, such as tin, silver, electroless nickel – immersion gold (ENIG), and electroless nickel – electroless palladium – immersion gold (ENEPIG) [8]-[10].

One issue that arose from increasing reflow temperature is excess warpage in components due to the coefficient of thermal expansion (CTE) mismatch between the encapsulation material and the substrate, as shown in Figure 1. Consequently, the reflow process can yield bridging solder joints, where adjacent solder joints are merged into a large solder joint, and head-in-pillow, where the solder balls of BGAs do not fully consolidate with the solder paste on the copper pad. Bridging solder joint creates unwanted shorts between IOs while head-in-pillow solder joint creates stress concentration on the solder joint, leading to reliability problems. To mitigate solder joint issues due to excess package warpage, methods have been developed to measure the warpage of packages during the reflow process [11]-[14].

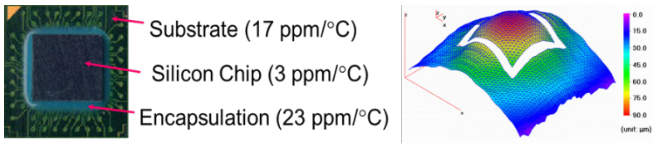

Figure 1: Warpage of Electronic Package at High Temperature During Reflow

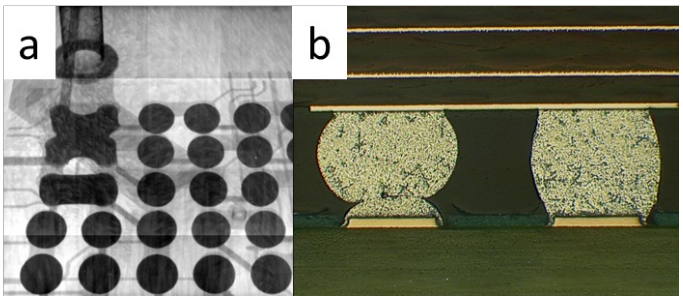

Figure 2: Warpage Defects a) Bridging Solder Joint, b) Head-in-Pillow Solder Joint

Provide Low and Stable Electrical Resistance for the Defined Life Time of the PCBA

The electrical performance of solder joints is based on electrical resistivity and the degradation of resistivity over time during operation. SAC alloys, with the presence of silver and copper have lower resistivity compared to SnPb, 13μΩ*cm compared to 14.5μΩ*cm [15]. Further, SAC solder experiences a small change in resistance under mechanical load and temperature cycling loads until failure [16]. This allows SAC305 solder to be accepted without much change to electrical performance consideration.

Survive Operation and Field Temperature Excursions for the Defined Life Time of the PCBA

Solder joints, in application, primarily experience two types of thermal excursions, heat generation from power cycle and environmental temperature. Under cyclic temperature excursions, temperature cycling or power cycling, the CTE mismatch between the package on the PCB or the thermal gradient causes cyclic strains on the solder joint. In addition, solder can creep when stressed at above homologous temperature (40% of the melting temperature in Kelvin) and continues to deform plastically without additional stress. The presence of both cyclic instantaneous plasticity and creep causes microstructural change, crack initiation, and crack propagation in solder joints [17]-[19].

Although the apparent failures of SAC solder and SnPb solder joints are complete cracks in the solder joints. The failure mechanism of SAC alloy and SnPb alloy are slightly different under cyclic

thermal excursion, as shown in Figure 3. Under temperature cycling, the Sn phase and Pb phase in SnPb enlarge near the high stress regions and the crack propagates between the enlarged phases. On the other hand, SAC solder joints under temperature form new small grains near the high stress regions through recrystallization and the crack propagation occurs between these newly formed finer grains.

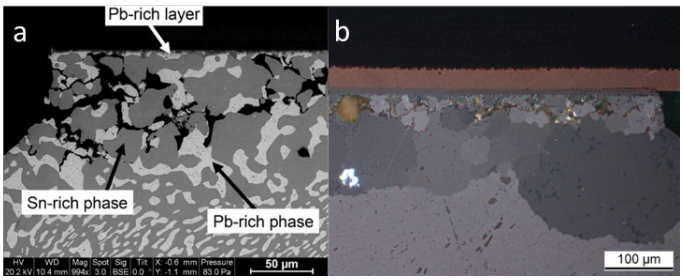

Figure 3: Temperature cycling failure mechanism: a) Tin and Lead phase enlargement for SnPb, b) recrystallization and small grain nucleation at high stress region for SAC305 solder

Despite the differences in failure mechanisms between SAC solder and SnPb, the reliability performance of SAC solder joints was one of the major points leading to SAC solder adoptions. Under accelerated temperature cycling tests, SAC305 solder outperforms SnPb solder every majority of the temperature cycling conditions listed in JEDEC standard except for extremely severe conditions where SnPb solder joints perform equally or better than SAC305 solder joints [20].

Although the temperature cycling reliability performance of SAC305 meets the need or surpasses SnPb in accelerated life tests, the question is how does SAC305 solder joint perform in real applications. To answer this question, fatigue models were developed to estimate the time to failure or reliability performance of solder joints in the field using existing accelerated life tests in the literature. Currently, there are three main fatigue life modeling approaches that are either a variation of Coffin-Manson's model [21] or Morrow's model [22]. One approach is the Norris-Landzberg model, that analytically calculates the acceleration factor between the field and test condition using environmental temperature conditions [23]. Another approach is Engelmaier's model, which estimates the fatigue lives of solder joints using the extrinsic and intrinsic properties of materials in the assembly and temperature cycling profiles [24]. Lastly, finite element analysis (FEA) approach, this approach estimates the strain or strain energy density in the solder joints using FEA shown in Figure 4 and correlate the strain and strain energy density with time to failure [25]. Regardless of the approaches, the available test data, fatigue models, and the understanding failure behavior of SAC helped the commercial industry to adopt SAC305.

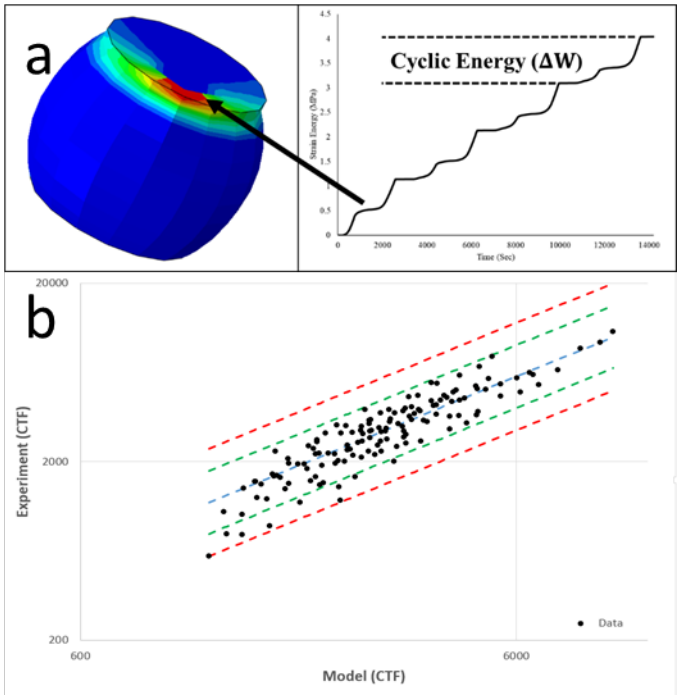

Figure 4: a) Strain energy density extraction from temperature cycling FEA, b) Model prediction vs test data

Surviving Operation and Field Mechanical Loads for the Defined Life Time of the PCBA

In addition to thermal excursions, solder joints can also experience mechanical loads such as vibration, shock/drop, torsion, and bending. Under mechanical loads, the stiffness differences between packages and the PCBs cause strains on solder joints. Such repetitive strain can lead crack initiation and crack propagation in solder joints. Furthermore, SAC305 solder is sensitive to strain rate, the rate at which strain is applied, increasing strain can increase the stiffness of the material. Increased stiffness in SAC305 solder joints relocates the weak link from solder joints to locations such as solder to copper pad intermetallic compound, copper traces, and PCB resin, as shown in Figure 5 [26]. While mixed failures such as bulk solder failure, IMC failure, copper trace failure, and pad cratering can be found in SAC305 interconnect under vibration loads, IMC, copper trace failure, and PCB pad cratering are the major failures found in SAC305 assemblies.

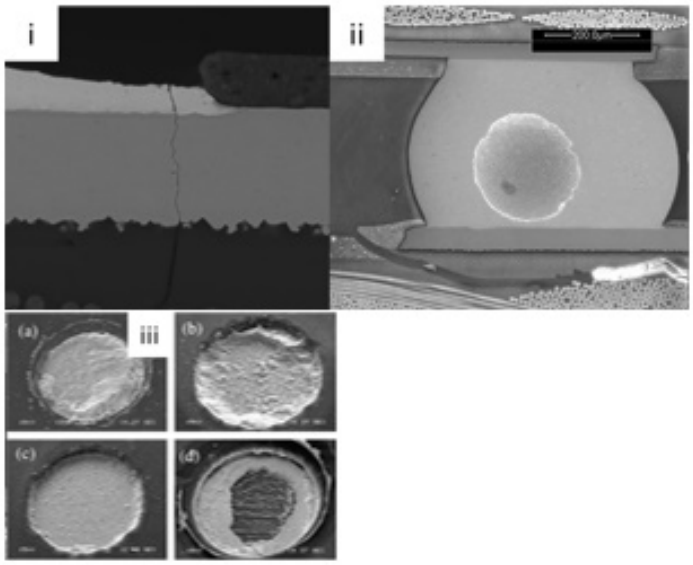

Figure 5: (i) Copper trace failure, (ii) PCB pad cratering, (iii) IMC failure under high strain rate mechanical tests

For SnPb solder and SAC solders, the majority of the reliability prediction methods are based on generalized Coffin Manson fatigue model [21][28]. Generally, drop, shock, bending, torsion yield failure due to low cycle fatigue and vibration yields failure under high cycle fatigue. Due to the complexity and the length scale of solder joints, the stress and strain on solder joints are estimated through finite element analysis while matching PCB strain between the FEA and the experiment. Fatigue model constants for both SnPb and SAC305 are well studied in the literature for both high cycle and low cycle fatigue [29].

One of the drawbacks of fatigue life estimation using FEA is time consuming. Thus, analytical models such as the Steinberg equation were developed for high cycle fatigue by assuming pure elastic deformation in solder [30]. Further, the IPC standard and MIL handbook suggest acceleration factor models that only consider the load levels, acceleration (G) or power spectral density, and high cycle fatigue model exponents [31][32]. The model constants are also available in the literature for SAC305 solder.

In general, SAC305 and SnPb perform similarly under high cycle fatigue or vibration loads, and SAC305 performs worse than SnPb under low cycle fatigue, particularly drop or shock [20]. The reason for the reduced low cycle fatigue life of SAC305 is its higher stiffness compared to SnPb, shifting failure sites to IMC, copper trace, and PCB. Studies were done in the late 2000s to improve shock reliability of SAC solders by reducing silver content, but the tradeoff was lowered temperature cycling fatigue life [33]. Another method of mitigating mechanical shock failures was using underfill or corner staking, where the correct selection of underfill and corner staking could significantly improve the mechanical shock reliability of SAC305 PCB assemblies [34].

Cornerstone Project

The United States Partnership for Assured Electronics (USPAE) has created the Defense Electronics Consortium (DEC) to address microelectronics research needs for the Department of Defense and the defense industrial base, including the aerospace electronics industry. The Solder Performance and Reliability Assurance (SPRA) project funded by Cornerstone OTA through the Industrial Base Analysis and Sustainment (IBAS) program is the first DEC project. The SPRA brings together the University of Maryland, Auburn University, Purdue University, and Binghamton University along with Collins Aerospace, Plexus, and STI Electronics, do develop a solder agnostic approach for qualifying solders for use in defense application. This five-year program will establish and demonstrate the process for qualifying solders for assembly and reliability with the development of life/acceleration models. In addition, the program will develop use case definitions with solder reliability qualification methods. The output of the program will be a solder users handbook and solder performance specification

CONCLUSION

This paper discussed the criteria for the adoption of SAC305 in the commercial microelectronic industry, including compatibility of SAC305 with the rest of the assembly and electrical performance and reliability under mechanical and thermal loads. The key factor for SAC305 adoption is superior or comparable fatigue performance of SAC305 compared to SnPb on top of the availability of fatigue life data and fatigue model constants for SAC305. Further, high strain rate failure mitigation methods such as underfill and corner staking help to improve the mechanical reliability of lead-free assemblies.

To adopt a new generation of lead-free solder, factors such as assembly compatibility, electrical performance, mechanical performance, thermal performance, and long-term reliability should be considered. Since the majority of the new generation solders for aerospace and defense industries are based on SAC alloys with additives, the melting temperature remains near 220°C, adopting a newer generation of solder requires less effort when it comes to PCBA compatibility. The major concern for new generation solders will be their reliability under various types of loads and this requires a large set of test data to provide the confidence for new solder adoption.

ACKNOWLEDGEMENTS

This paper was supported Solder Performance and Reliability Assurance (SPRA) project funded through the United States Partnership for Assured Electronics (USPAE) by Cornerstone Initiate Request (CIR) CS-20-1302 for Lead-Free Defense Electronics.

REFERENCES

[1] "Directive 2002/95/EC of the European Parliament and of the Council of 27 January 2003 on the restriction of the use of certain hazardous substances in electrical and electronic equipment", Official Journal L 037, pp. 19-23, February 13, 2003, Accessed online: http://eur-lex.europa.eu/LexUriServ/LexUriServ.do?uri=CELEX:32002L0095:EN:HTML, Last accessed: Oct 12, 2014.

[2] Iyer, Ganesh, Eric Ouyang, Witoon Kittidacha, Soratos Tantideeravit, and L. K. Suresh. "Pb-free solder: SAC105 vs SAC305 drop-test reliability data comparison." In 2007 32nd IEEE/CPMT International Electronic Manufacturing Technology Symposium, pp. 251-255. IEEE, 2007.

[3] Sweatman, Keith, Richard Coyle, Richard Parker, Keith Howell, Elizabeth Benedetto, Joseph Smetana, Aileen Allen, Weiping Lui, and Julie Silk. "iNEMI PB-FREE ALLOY CHARACTERIZATION PROJECT REPORT: PART VII-THERMAL FATIGUE RESULTS FOR LOW-AG ALLOYS." (2014).

[4] Coyle, Richard J. "Lead (Pb)-free solders for high reliability and high-performance applications." Lead-free Soldering Process Development and Reliability (2020): 191-247.

[5] Che, F. X., John HL Pang, B. S. Xiong, Luhua Xu, and T. H. Low. "Lead-free solder joint reliability characterization for PBGA, PQFP and TSSOP assemblies." In Proceedings Electronic Components and Technology, 2005. ECTC'05., pp. 916-921. IEEE, 2005.

[6] Ren, Guang, Ian J. Wilding, and Maurice N. Collins. "Alloying influences on low melt temperature SnZn and SnBi solder alloys for electronic interconnections." Journal of Alloys and Compounds 665 (2016): 251-260.

[7] Fu, Haley, Raiyo Aspandiar, Jimmy Chen, Shunfeng Cheng, Qin Chen, Richard Coyle, Sophia Feng et al. "INEMI project on process development of BISN-based low temperature solder pastes—Part II: characterization of mixed alloy BGA solder joints." In 2018 Pan Pacific Microelectronics Symposium (Pan Pacific), pp. 1-17. IEEE, 2018.

[8] Collins, Maurice N., Jeff Punch, and Richard Coyle. "Surface finish effect on reliability of SAC 305 soldered chip resistors." Soldering & Surface Mount Technology (2012).

[9] Huang, Meng-Kuang, Chiapyng Lee, Pei-Lin Wu, and Shyh-Rong Tzan. "The effects of surface finish on the reliability of lead-free and tin lead chip scale package solder joints." Soldering & surface mount technology (2005).

[10] Yang, Se Young, Young-Doo Jeon, Soon-Bok Lee, and Kyung-Wook Paik. "Solder reflow process induced residual warpage measurement and its influence on reliability of flip-chip electronic packages." Microelectronics Reliability 46, no. 2-4 (2006): 512-522.

[11] Li, Li, Ken Hubbard, and Jie Xue. "Improving board assembly yield through PBGA warpage reduction." In 2009 International Conference on Electronic Packaging Technology & High Density Packaging, pp. 949-953. IEEE, 2009.

[12] Tsai, Ming-Yi, Yu-C. Chen, and SW Ricky Lee. "Correlation between measurement and simulation of thermal warpage in PBGA with consideration of molding compound residual strain." IEEE Transactions on Components and Packaging Technologies 31, no. 3 (2008): 683-690.

[13] Yang, Se Young, Young-Doo Jeon, Soon-Bok Lee, and Kyung-Wook Paik. "Solder reflow process induced residual warpage measurement and its influence on reliability of flip-chip electronic packages." Microelectronics Reliability 46, no. 2-4 (2006): 512-522.

[14] Tsai, Ming-Yi, Hsing-Yu Chang, and Michael Pecht. "Warpage analysis of flip-chip PBGA packages subject to thermal loading." IEEE Transactions on Device and Materials Reliability 9, no. 3 (2009): 419-424.

[15] N. D. Codreanu et al., "SAC Alloys Implementation in Electronic Products Manufacturing," 2006 29th International Spring Seminar on Electronics Technology, 2006, pp. 444-449

[16] Caers, J. F. J., E. H. Wong, S. K. W. Seah, X. J. Zhao, C. S. Selvanayagam, W. D. van Driel, N. Owens et al. "A study of crack propagation in Pb-free solder joints under drop impact." In 2008 58th Electronic Components and Technology Conference, pp. 1166-1172. IEEE, 2008.

[17] Dasgupta, A., C. Oyan, D. Barker, and M. Pecht. "Solder creep-fatigue analysis by an energy-partitioning approach." (1992): 152-160.

[18] Sundelin, Janne J., Sami T. Nurmi, and Toivo K. Lepistö. "Recrystallization behaviour of SnAgCu solder joints." Materials Science and Engineering: A 474, no. 1-2 (2008): 201-207.

[19] Yin, Liang, Luke Wentlent, Linlin Yang, Babak Arfaei, Awni Oasaimeh, and Peter Borgesen. "Recrystallization and precipitate coarsening in Pb-free solder joints during thermomechanical fatigue." Journal of electronic materials 41, no. 2 (2012): 241-252.

[20] Osterman, Michael, and Abhijit Dasgupta. "Life expectancies of Pb-free SAC solder interconnects in electronic hardware." In Lead-Free Electronic Solders, pp. 229-236. Springer, Boston, MA, 2006.

[21] S. S. Manson, Thermal Stress and Low Cycle Fatigue, Hew York:McGraw-Hill, 1966.

[22] J. Morrow, "Cyclic plastic strain energy and fatigue of metals," in Proceeding of Symposium in Internal Friction, Damping, and Cyclic Plasticity, ASTM, (STP-378)

[23] Norris, K. C., and Landzberg, A. H., 1969, "Reliability of Controlled Collapse Interconnections," IBM J. Res. Dev., 13, pp. 266–271

[24] Engelmaier, W. "Functional cycles and surface mounting attachment reliability." Circuit World (1985).

[25] Chen, Deng Yun, Michael Osterman, and Abhijit Dasgupta. "Energy based modeling for temperature cycling induced tin silver copper solder interconnect fatigue life." Microelectronics Reliability 109 (2020): 113651.

[26] Wong, Ee-Hua, S. K. W. Seah, and V. P. W. Shim. "A review of board level solder joints for mobile applications." Microelectronics Reliability 48, no. 11-12 (2008): 1747-1758.

[27] Dasgupta, A., C. Oyan, D. Barker, and M. Pecht. "Solder creep-fatigue analysis by an energy-partitioning approach." (1992): 152-160.

[28] Basquin, O. H. "The exponential law of endurance test". Proceedings of the American Society for Testing and Materials. (1910): 625–630.

[29] Zhou, Yuxun, M. Al-Bassyiouni, and A. Dasgupta. "Vibration durability assessment of Sn3. 0Ag0. 5Cu and Sn37Pb solders under harmonic excitation." (2009): 011016.

[30] Steinberg, Dave S. "Vibration analysis for electronic equipment." (2000).

[31] IPC-SM-785. Guidelines for accelerated reliability testing of surface mount solder attachments

[32] MIL-STD-810G w/Change 1, Environmental Engineering Considerations and Laboratory Tests; U.S. Department of Defense: Washington, DC, USA, 2014.

[33] Iyer, Ganesh, Eric Ouyang, Witoon Kittidacha, Soratos Tantideeravit, and L. K. Suresh. "Pb-free solder: SAC105 vs SAC305 drop-test reliability data comparison." In 2007 32nd IEEE/CPMT International Electronic Manufacturing Technology Symposium, pp. 251-255. IEEE, 2007.

[34] Chheda, Bankeem V., S. Manian Ramkumar, and Reza Ghaffarian. "Thermal shock and drop test performance of lead-free assemblies with no-underfill, corner-underfill and full-underfill." In 2010 Proceedings 60th Electronic Components and Technology Conference (ECTC), pp. 935-942. IEEE, 2010.

[35] Cucu, Traian C., Norocel-Dragos Codreanu, and I. Plotog. "Reflow process using lead-free materials-basics and comparison with tin-lead process." In Proceedings of the 2005 Interntional Symposium for Design Technology and Electronics Packaging (SIITME 2005), Cluj-Napoca, Romania, pp. 250-255. 2005.

Conformal Coating Testing in Various Test Environments

P. Singh[1], L. Palmer[1], C. Xu[2], J. Kaufman[2], H. Fu[3], S. Strixner[4], H. Schweigart[4], M. R. Meier[4], C. Wang[5], M. Pudas[6], M Smith[7], J. Payne[7], H. Remore[7], M. Zhai[8], S. Calvelli[8,9], H. Shi[8], A. Locquet[8], D. S. Citrin[8], D. Hampannavar[10], M. M. Khaw[11], K-L Tan[11] and H. Akbari[12]

[1]IBM Corp, NY, USA, [2]Nokia, NJ, USA, [3]iNEMI, Shanghai, China, [4]Zestron Europe, Germany, [5]Zestron China, Shanghai, China, [6]Picosun Oy, Espoo, Finland, [7]3M, MN, USA, [8]Georgia Tech, Atlanta, USA, [9]University of Calabria, Italy, [10]HP, Bangaluru, India, [11]Keysight, Penang, Malaysia, [12]Schlumberger, TX, USA

ABSTRACT

Conformal coatings have traditionally been tested by determining the mean time to failure of conformally coated hardware exposed to corrosive test environments. This test approach has serious shortcomings: The test temperatures are most often too high. At these high temperatures, the conformal coating properties may be quite different from those at the application temperatures. In addition, the times to failure are unacceptably long extending into many months. Overcoming these shortcomings is an iNEMI championed test that involves exposing conformally coated thin films of copper and silver to sulfur vapors at 40-50 °C in flowers of sulfur (FoS) chamber and using the corrosion rates of the coated metal thin films as a measure of the corrosion protection capabilities of the conformal coatings. The test temperatures are similar to the application temperatures, the test durations are no more than a week and can be conducted under various temperature and humidity conditions. The purpose of this paper was to determine if testing in the industry-standard mixed-flowing gas corrosion chamber would give similar results as those using the FoS chamber. Acrylic, fluorinated acrylate, and atomic layer deposition conformal coatings were tested in three environments: (a) flowers of sulfur (FoS), (b) mixed-flowing gas (MFG), and (c) iodine vapor. The performance of the coatings tested in the FoS and the MFG corrosion chambers were quantitatively similar. The iodine vapor test results were in qualitative agreement with the FoS and MFG test results.

INTRODUCTION

Conformal coatings protect coated hardware from the ill effects of moisture, dust, and corrosive gases. With ever-expanding markets for electronic goods, the world over, in environments ranging from benign to very harsh, the need for conformal coatings is ever increasing. Given a wide range of available conformal coatings and given a multitude of hardware on which they need to be applied, it behoves the industry to have standardized means of testing conformal coatings under the various application conditions.

Until recently, it was typical to test conformal coatings by applying them to actual hardware and determining the mean time to failure at high temperatures in the neighbourhood of 100°C in corrosive, generally flowers of sulfur, environments [1]. This approach suffers two shortcomings: One is that the conformal coating properties at high-test temperatures may be very different from those at the application temperatures; the other is that the test times are too long, extending into many months and sometimes longer. An iNEMI championed novel test approach overcomes these shortcomings by applying the coatings to metal thin films and characterizing the conformal coatings by the degree of corrosion protection they provide the underlying metal thin films [2]. The test temperatures are similar to the application temperatures and the test durations are as short as one week. In the first phase of the iNEMI project that studied this approach, testing was conducted in flowers of sulphur (FoS) chambers. Given that the industry-accepted environment for testing electronic hardware is the mixed-flowing gas (MFG) environment, iNEMI embarked on phase 2 of the project to compare conformal coating test results from testing in the FoS environment to those in the MFG environment. The iodine vapour test environment was included as the third environment in the project [3].

This paper compared these three environments in terms of how well they characterize conformal coatings. The conformal coatings chosen for testing provided a range of corrosion protection to the underlying metal thin films: acrylic coating provided moderate corrosion protection; fluorinated acrylate coating provided improved corrosion protection and the atomic layer deposited (ALD) coating provided excellent corrosion protection. The FoS and the MFG tests provided quantitatively similar results on the corrosion protection abilities of the conformal coatings. The iodine vapor test, taking no more than an hour to conduct, provided qualitative corrosion characterization of the coatings that agreed with the results of the FoS and the MFG tests.

TEST METHODS

Conformal coatings were quantitatively characterized by the degree of corrosion protection the coatings provided the underlying, 800-nm thick silver and copper serpentine thin films when exposed to corrosive FoS or MFG environments. Figure 1 illustrates a metal thin-film test coupon as a serpentine metal thin film deposited on silicon oxide on silicon mounted on a pegboard with 4-point resistance measurement connections to a receptable connector. Conformal coatings were characterized by comparing the corrosion rates of the coated metal thin films to those of uncoated, bare metal thin films. The corrosion rates of the thin films in the FoS and the MFG environments were measured electrically via the rates of resistance increase of the films. Thin film electrical resistances were measured via the 4-point resistance method, in galvanostatic mode, in which known currents were pumped through the thin films and the potential drops across them measured. Tests were run in low (10%), medium (32-34%) and high (70-75%) relative humidity environments at 30°C in the MFG test chamber and at 40°C in the FoS test chamber.

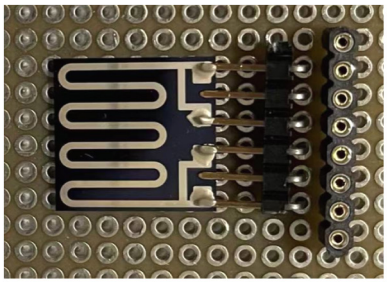

(a)

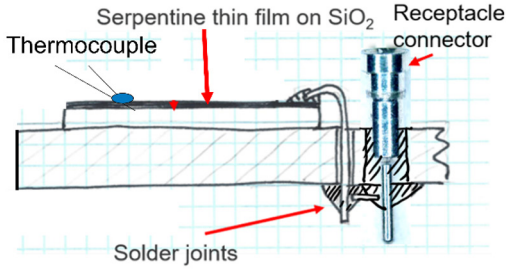

(b)

Figure 1: Thin-film test coupon showing (a) silver serpentine thin film on SiO2/Si mounted on a circuit board and (b) schematic of cross-section of test coupon showing the way to connect the thin film to the receptacle connector.

The FoS chamber setup is described in Figure 2. The corrosive gas in the FoS chamber was sulfur gas with its concentration kept constant by keeping the chamber temperature constant. The relative humidity in the chamber was kept constant using a saturated salt solution with its deliquescent relative humidity matching the desired relative humidity. The thin films and the coatings housed in a FoS chamber at 40°C were heated to and kept constant at various temperatures as high as 75°C, using joule heating. The currents used to measure the film resistances were also used to joule heat the thin films and the conformal coatings covering them. The temperatures of the coatings were measured using 50-µm diameter T-type thermocouples glued to the coatings. The testing in an industry standard MFG chamber was like that in the FoS chamber with a couple of differences. The MFG chamber was held at 30°C and the gas composition was 200 ppb SO_2; 100 ppb H_2S; 200 ppb NO_x and 20 ppb Cl_2.

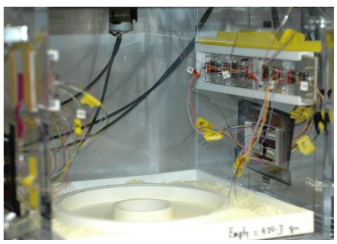

(a)

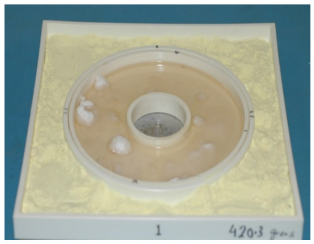

(b)

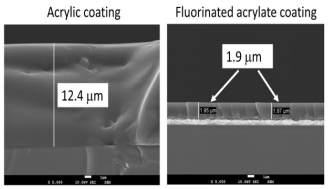

(c)

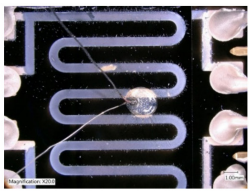

(d)

Figure 2: FoS chamber test setup showing (a) the inside of the chamber with thin films mounted on the chamber walls and sulfur and saturated salt trays on the bottom; (b) the flowers of sulfur tray surrounding the saturated salt solution tray; (c) cross sections of acrylic and fluorinated acylate coatings, and (d) enlarged view of a silver serpentine thin film showing the thermocouple bonded to the surface adjacent to the thin film.

The corrosivity of the FoS and MFG environments were measured by measuring the corrosion rates of bare copper and bare silver thin films and foils. The thin metal film corrosion rates were measured using the rates of electrical resistance increase method. The metal foil corrosion rates were measured either by the mass gain method or by coulometric reduction [4]. Figure 3 summarized these corrosion rates as a function of relative humidity. The corrosion rates of thin metal films are in general higher than those of metal foils because thin films have finer gain size and have higher internal mechanical stresses.

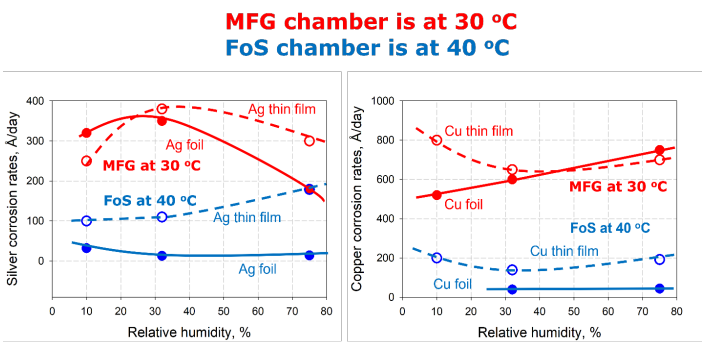

Figure 3: Corrosion rates of bare copper and bare silver thin films and metal foils in MFG and FoS chambers as a function of relative humidity were used to characterize the corrosivity of the chamber environments.

The iodine vapor test involved exposing coated serpentine metal thin films to iodine vapor at 40°C and 100% relative humidity for 30 and 60 minutes and optically estimating the extent of the metal film corrosion. The test setup is shown in Fig. 4a and 4b. The iodine vapors that come off an iodine saturated aqueous solution at 70°C in a sealed container are at 40°C, as is evident in the graph of Fig. 4c.

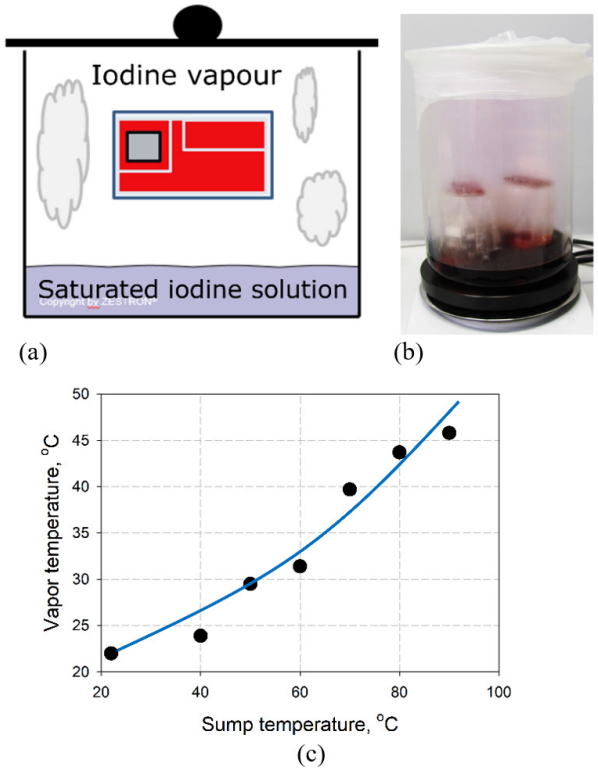

Figure 4: Description of the iodine vapor test: (a) Schematic of the setup; (b) Test chamber; (c) Plot showing that at 70°C sump temperature, the vapor temperature was 40°C. The relative humidity in the chamber was 100%.

In the FoS and the MFG chambers, the extents of the corrosion of bare and of conformally coated copper and silver thin films were measured as a function of time at various conformal coating temperatures. The corrosion rates at various coating temperatures were obtained from the slopes of these plots.

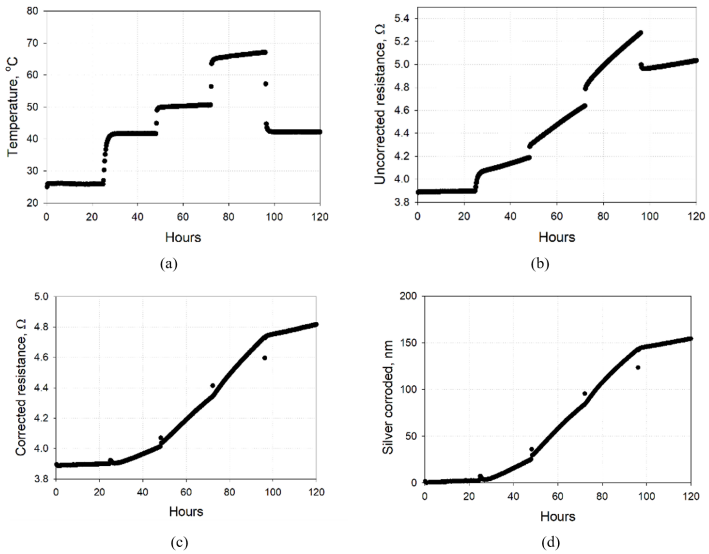

Figure 5: Steps are shown to obtain the thickness of silver corroded as a function of time. This example is for bare silver corroding in 40°C, 10% relative humidity environment. The thin-film temperature was stepped to various values by joule heating the film.

The steps followed to determine the thickness of metal film corroded away as a function of time during five periods, each period at a constant temperature lasting one day in the FoS test, are shown in Fig. 5. The periods were shorter in the MFG test (4 to 16 hours) because of the higher corrosion rates in the MFG environment. The example shown in Fig. 5 is for testing in the FoS environment. During the first period which was the first day in the FoS test, the test chamber was at room temperature. For the remaining four periods, each lasting a day in the FoS test, the chamber temperature was raised to and held constant at 40°C. During day 2, the joule heating resulting from 100-mA current raised the film temperature slightly above the ambient to about 42°C; during day 3, the 200-mA current raised the film temperature to about 52°C; during day 4, the 300-mA current raised the film temperature to about 68°C; and during day 5, the 100-mA current lowered the film temperature to about 43°C. The jogs in the as-measured resistance plot, shown in Fig 5b, we term "uncorrected" resistance, at the instant of change of temperature of the film, were the direct result of the temperature coefficient of electrical resistivity of the metal films. We can compensate for this effect by calculating what would be the film resistance if the film was to be cooled to 40°C. This corrected film resistance, with the jogs smoothened out, is plotted in Fig. 5c. Knowing that the film thickness is inversely proportional to its electrical resistance, the thickness of metal film corroded away can be calculated. The above-described procedure was repeated in

low, medium, and high relative humidity ambiences at 40°C in FoS and at 30°C in MFG environments, on copper and silver thin films coated with the three coatings under test along with the uncoated thin films.

RESULTS AND DISCUSSION

An example of coated and uncoated silver and copper thin films corrosion in the FoS chamber is shown in Fig. 6 for 32% relative humidity and 40°C test run. The plots of the thickness of silver and copper corroded versus time have almost no jogs associated with temperature changes, indicating well-chosen values of the silver and copper coefficients of electrical resistivities. Anyway, it was discovered that the selected coefficients of resistivity values had little effect on the calculated corrosion rates. From the slopes of a metal corroded plot (Fig 7a) at various temperatures, the corrosion rates can be obtained and plotted in an Arrhenius fashion as shown in Fig. 7b.

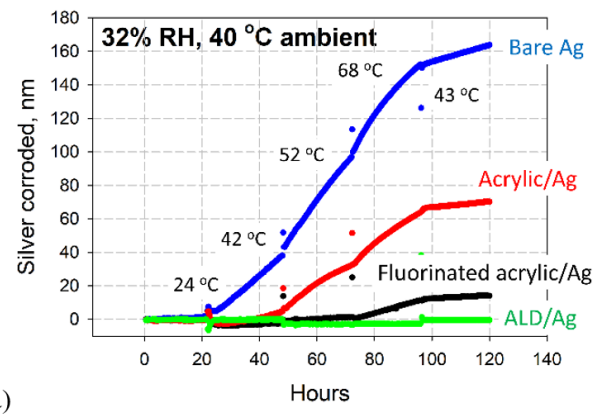

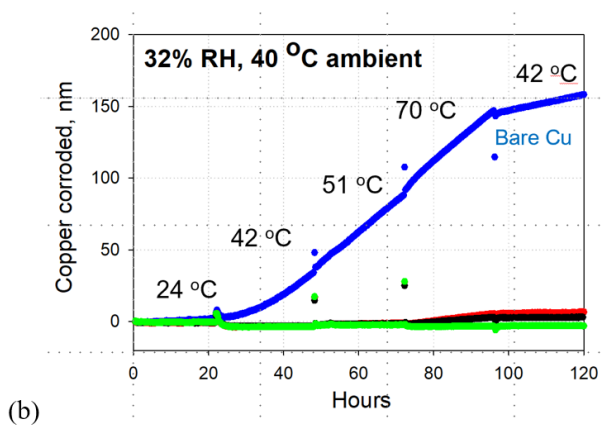

Figure 6: Example of corrosion in FoS chamber at 32% relative humidity and 40°C. (a) Thickness of Ag corroded; (b) Thickness of Cu corroded. Note the low corrosion rates of coated Cu compared to coated Ag, even though the coated Cu and Ag film corrosion rates were similar.

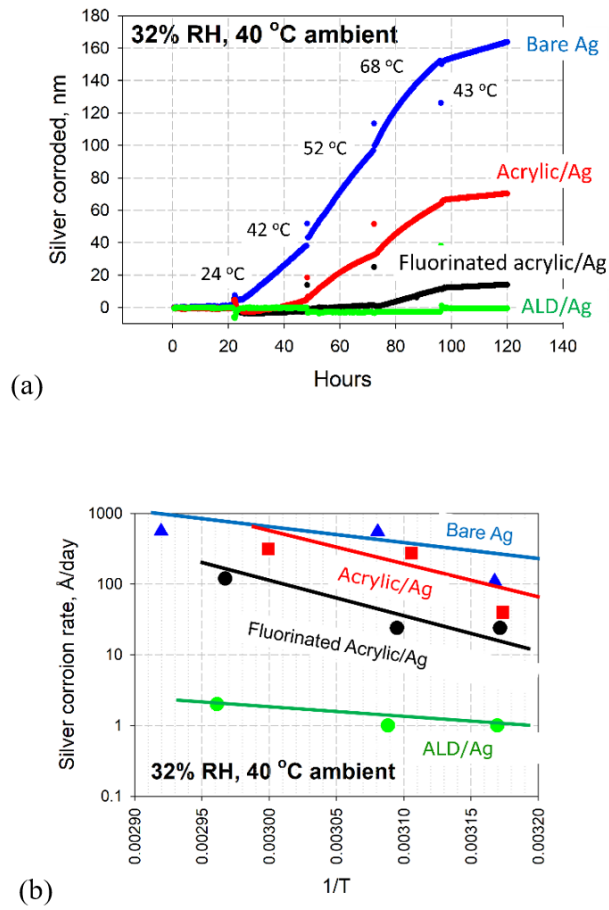

Figure 7: Example of converting thickness of silver corroded vs time at various temperatures into an Arrhenius pot.

Before summarizing/displaying the data on Arrhenius plots, it is worth delving into the advantage of Arrhenius plots : They allow a wide range of corrosion rates stretching over many orders of magnitude to be plotted on one plot and equally importantly the slopes of the plots shed light on the rates of corrosive gas transport through the conformal coatings and the reaction rates between the gases and the metal. Data lying on a linear plot with no break in slope indicates one controlling mechanism, whereas a change in slope indicates changing mechanisms over the temperature range of measurement. Fig. 8 and 9 capture the corrosion rates data of coated and uncoated silver and copper thin films over three orders of magnitude of corrosion rates. However, the standard deviations of the corrosion rates are too high to be of use in discussions on the mass transport mechanisms and reaction rates at the metal thin film surfaces. The purpose and discussion of the Arrhenius plots in the following paragraphs are therefore generally limited to the concise presentation of corrosion rate data rather than the mass transport and chemical reaction rates and their mechanisms and the associated activation energies.

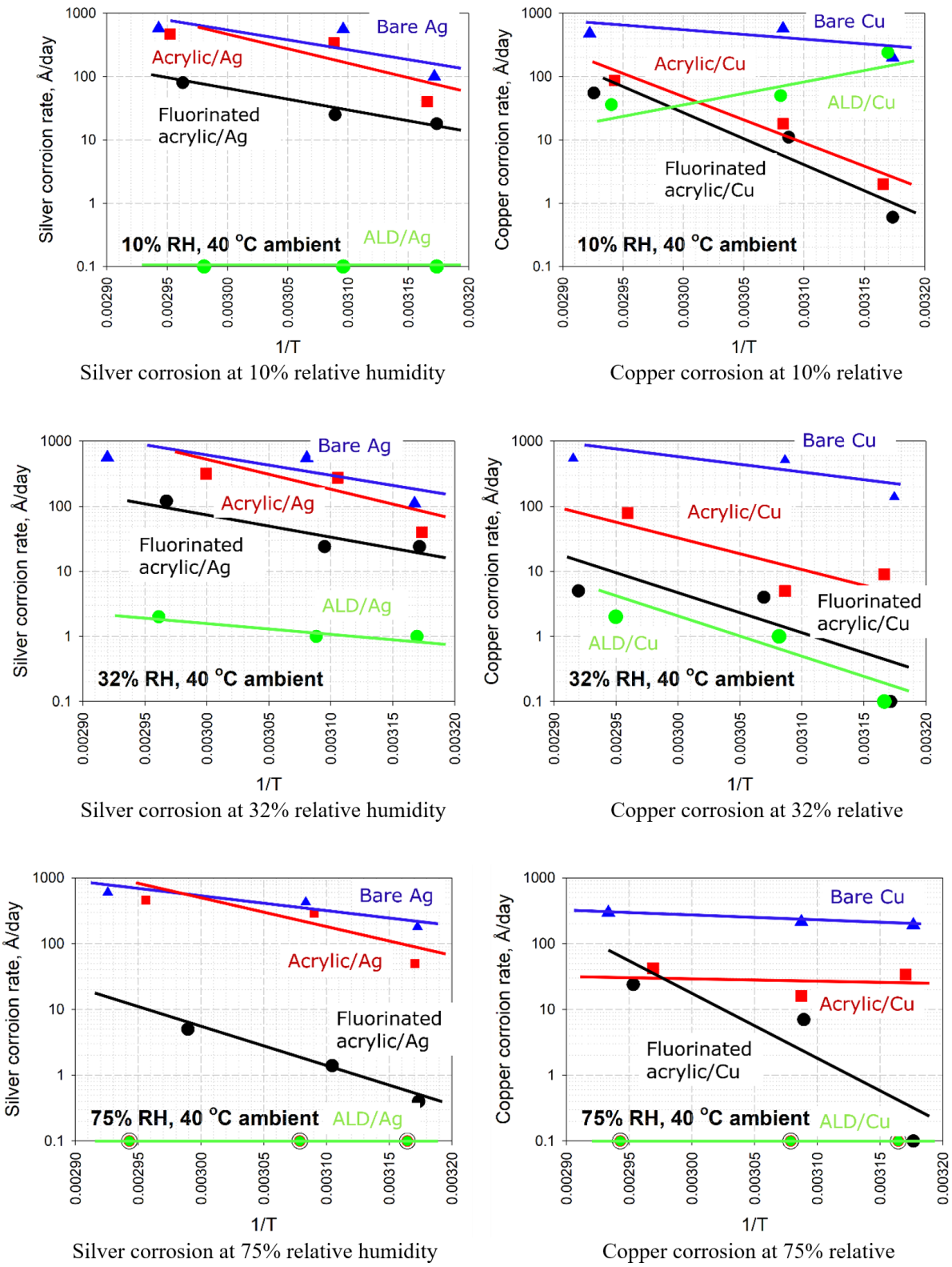

Figure 8: Arrhenius plots of silver and copper corrosion rates in FoS chamber at various relative humidity levels at 40°C chamber temperature.

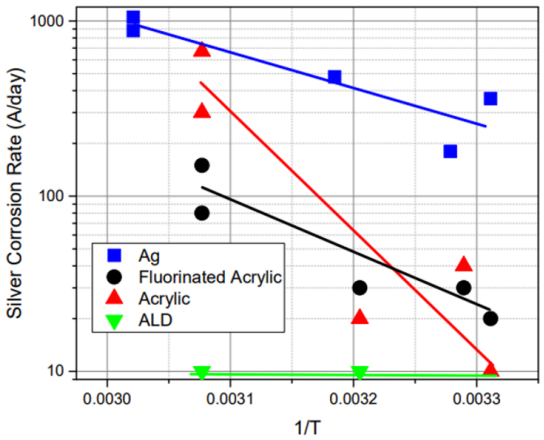

Silver corrosion at 10% relative humidity

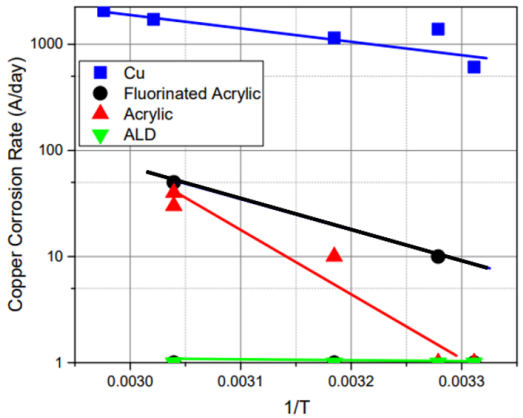

Copper corrosion at 10% relative humidity

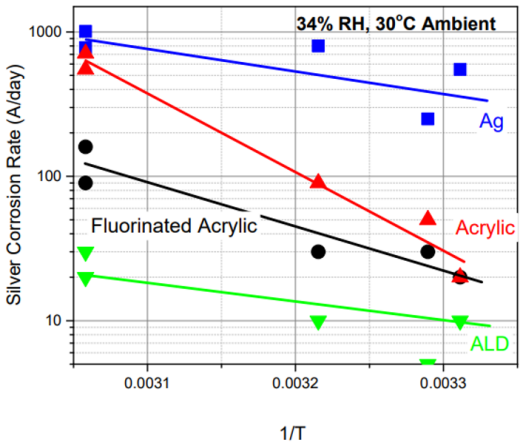

Silver corrosion at 34% relative humidity

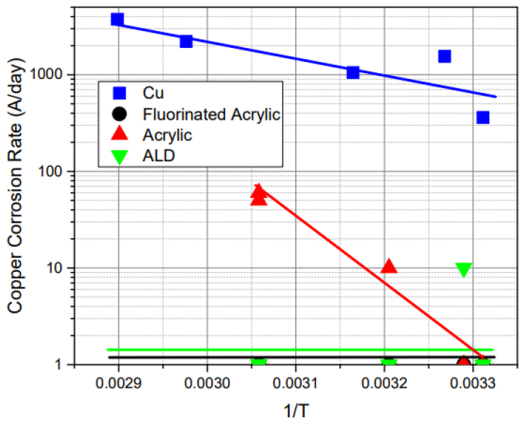

Copper corrosion at 34% relative humidity

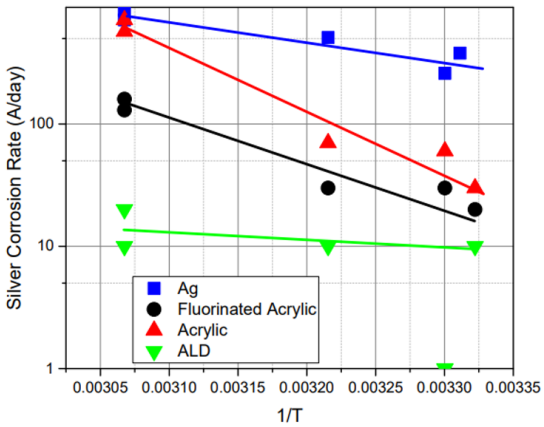

Silver corrosion at 70% relative humidity

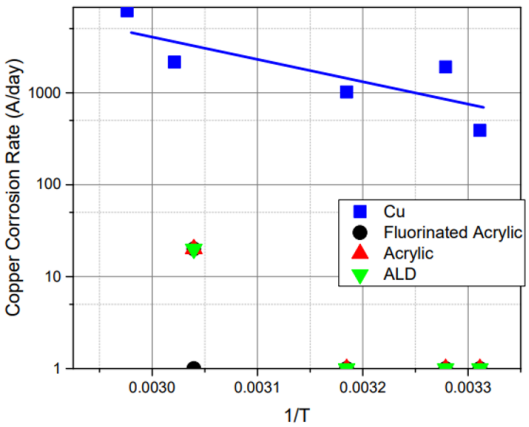

Copper corrosion at 70% relative humidity

Figure 9: Arrhenius plots of silver and copper corrosion rates in MFG chamber at various relative humidity levels at 30°C chamber temperature.

Table 1: Iodine vapor test results

Coating	Thin film	After 30 minutes in iodine vapors	After 60 minutes in iodine vapor
Acrylic	Ag	Corroded except at the edge where the coating was thicker	Fully corroded
	Cu	No corrosion	Corrosion occurred except in areas of thicker coating
Fluorinated acrylate	Ag	Corroded	Corroded
	Cu	Corrosion started	Corrosion progressed
ALD	Ag	No corrosion	Corrosion started on the edges
	Cu	Slight corrosion	Corrosion proceeded

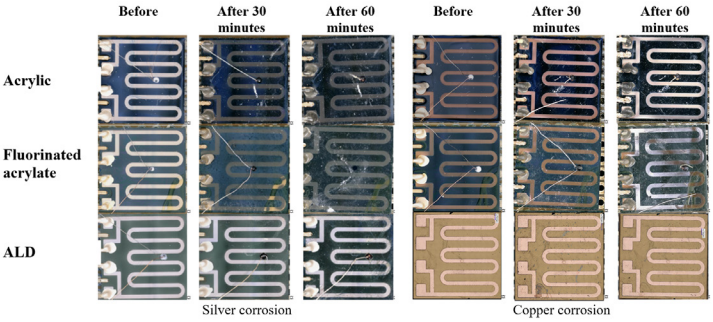

Figure 10: Visual inspection of the coated thin films subjected to iodine vapors for 30 and 60 minutes under a low magnification microscope indicates that the thin films under the acrylic coatings corroded the most, the fluorinated acrylate coated thin films corroded less and the ALD coated thin films corroded the least. The ALD-coated thin copper films look different because the thin films were precleaned before the deposition of the ALD coating.

The corrosion rates of uncoated and coated copper and silver thin films in 10, 32, and 75% relative humidity FoS environments are summarized in the Arrhenius plots of Figure 8. Notice that in general the corrosion rates of coated copper thin films are less than those of coated silver thin films indicating that copper is better protected from corrosion by the conformal coatings.

The corrosion rates of uncoated and coated copper and silver thin firms in 10, 34, and 70% relative humidity MFG environments are summarized in the Arrhenius plots of Figure 9. Notice that, in this case too, in general, the corrosion rates of coated copper thin films are less than those of coated silver tin films indicating that copper is better protected from corrosion by the conformal coatings.

As expected by the more corrosive environment in the MFG chamber, the corrosion rates of uncoated and coated thin films were in general higher in the MFG chamber compared to in the FoS chamber; though the results from the coatings tested in the two environments trend in a similar manner: The ALD coating provided the best corrosion protection to the coated metal film; the fluorinated acrylate the next best protection and the acrylic coating provided lesser protection.

The relatively linear nature of the Arrhenius plots of Figs. 8 and 9 indicate that the transport mechanism of corrosive chemical species through the conformal coatings remains the same over the 40 to 75 °C range of temperature employed in this study. In both the FoS and the MFG tests, the temperature had a strong degrading effect on the acrylic and the fluorinated acrylate coatings. The corrosion rates of the ALD coatings were too low to observe any temperature effects.

The iodine vapor test results are shown in Fig. 10 for silver and copper thin films and are tabulated in Table 1. Silver and copper thin films under the ALD coatings corroded the least; the films corroded a little more under the fluorinated acrylate coatings and the most under the acrylic coatings, in agreement with the test results in the FoS and the MFG chambers.

CONCLUSIONS

The flowers of sulfur (FoS) and the mixed-flowing gas (MFG) test results were in quantitative agreement in their characterization of the corrosion protection provided by the acrylic, the fluorinated acrylate, and the atomic layer deposited coatings. The coatings tested provided much better corrosion protection to the underlying copper than to silver, probably because of the better adhesion of the coatings to copper.

The FoS chamber is of simple construction, and easy to operate [5]. It is a couple of orders of magnitude less expensive to own and operate compared to the MFG chamber. This study demonstrated that the FoS chamber is as effective an environment as the industry standard MFG chamber in testing conformal coatings. The iodine vapor test can be done in an hour. Its characterization of conformal coatings is in qualitative agreement with the results from the FoS and the MFG tests.

REFERENCES

[1] M. Cole, J. Porter, J. Wertz, M. Coq, J. Wilcox, and M. Meilunas, "Conformal coatings in preventing resistor silver sulfide corrosion," Proceedings of SMTA Int'l, Rosemont, IL, USA, 25-29 Sept 2016.

[2] P. Singh, L. Palmer, and M. Gaynes, "Conformal coating characterization using stacked silver thin films," 2020 SMTA Int'l Pan Pacific Symposium, Hi, USA, 10-13 Feb 2020.

[3] M. R. Meier, and H. Schweigart, "Quality test for potting materials regarding susceptibility to harmful gases and humidity," EBL 2020 - Elektronische Baugruppen und Leiterplatten conference, Germany, 18-19 Feb 2020.

[4] S. J. Krumbein, B. Newell, and V. Pascucci, "Monitoring environmental tests by coulometric reduction of metallic control samples," Journal of Testing and Evaluation, ASTM 1989.

[5] P. Singh, H. Fu, C. Xu, S. Lee, L. Palmer, D. Lee, K. Guo, J. Liu, "iNEMI general purpose FoS corrosion chamber," IPC APEX Expo, San Diego, CA, 2019

BIOGRAPHIES

Prabjit Singh is a Senior Technical Staff Member in IBM Poughkeepsie, with 45 years of experience in the metallurgical engineering aspects of mainframe computer power, packaging, cooling and reliability. For many years he taught a graduate course on Power Electronics at The State University of New York at New Paltz. He authored the ASHRAE book on data center gaseous and particulate contamination. He has 88 issued patents and is an IBM Master Inventor. He is a Distinguished Alumnus of the Indian Institute of Technology and an iNEMI Fellow. He received B.Tech. degree in Metallurgical Engineering from the Indian Institute of Technology in 1969 followed by a M.S. and a Ph.D. in Metallurgy from the Stevens Institute of Technology, Hoboken, New Jersey, in 1973 and 1977. Later he received a M.S. in Micro-Electronic Manufacturing from the Rensselaer Polytechnic Institute, Troy, New York, and a M.S. in Electrical Engineering from Walden University, Minneapolis.

Dr. Chen Xu is a Distinguished Member of Technical Staff with Nokia Bell Labs CTO. He has extensive experience in the fields of semiconductor and electronic packaging, electronic manufacturing, surface finishes and coatings, failure mode analysis and reliability assessment. In the last 15 years, he has been focusing on the impact of environmental conditions (such as corrosive, dusty and salty environments) on the reliability and performance of electronic equipment. Chen Xu received his BS Degree in Chemistry from Tong-ji University in Shanghai, China and his Ph.D. in Physical Chemistry from Ruhr-University Bochum, Germany.

Deepak Hampannavar is working as a Reliability Engineer IV with hp Inc in Bangalore, India. He holds ASQ Certified Reliability Engineer (CRE), Certified Quality Auditor (CQA), Certified Six Sigma Green Belt (CSSGB) and NAFI Certified Fire and Explosion Investigator (CFEI) Certifications. He is actively involved in Reliability, Failure Analysis, Design for Environment and Quality Assurance of hp products in the India region.

Khaw Mei Ming holds a bachelor's degree in Electronics and Computer Engineering and boasts 25 years of PCA manufacturing expertise in the EMS and OEM sector. She is certified by BSI as a Lean Sigma Black Belt, overseeing Keysight's Corporate PCB/PCA design guidelines and quality acceptance standards.

Marko Pudas received his M.Sc. degree in Chemistry and Doctorate degree Electronic manufacturing at University of Oulu. He has worked 10y with ALD, on applications such as corrosion and tin whiskers mitigation. He has contributed to >50 publications and >50 patents families.

Hossein Akbari is a project manager with Schlumberger in Katy, TX. Hossein received his Master's degree in Polymer Science from Martin Luther University in Germany and joined Schlumberger in 2006. He has had different assignments in Technology Centres based in Europe and the USA. Throughout his career Hossein has mainly worked on product development, tool architecture, material and processing. His speciality is material science, process optimization, failure analysis and unconventional testing.

Effect of Matte-Sn Electroplating Parameters on the Thermo-mechanical Reliability of Lead-free Solder Joints

Abhilaash Ajith Kumar and Werner Hügel, Ph.D.
Robert Bosch GmbH
Schwieberdingen, Germany

ABSTRACT

The Most of the Cu/Cu alloy lead-frames of electronic components used for automotive applications contain electroplated matte-Sn terminal finish to improve the wettability of Sn-based Pb-free solders during reflow soldering process. When the solder joints are subjected to combined thermal and mechanical cyclic loading, the influence of matte-Sn electroplating parameters can lead to early and brittle failure of the solder joint. To test this hypothesis, a factorial design of experiments (DOE) has been conducted with LFPAK-MOSFET (hereafter referred to as LFPAK) components plated with different matte-Sn electroplating parameters and reflow soldered with two solder alloys (SAC 305 and Innolot). The LFPAK solder joints were then subjected to thermo-mechanical in-phase cyclic loading under different strain amplitudes. No electrical measurement is done to eradicate the effect of electrical current on the solder joint. The response to the DOE is the crack percentage obtained in the LFPAK solder joints after 1000 and 2000 cycles. The Innolot solder joints exhibited lower crack percentages than the SAC 305. The level of organic additives in the electroplating process of matte-Sn influences the failure mode of the solder joint. Microstructural investigation attributes the nature of failure to the morphology of the $(Cu,Ni)_6Sn_5$ IMC phase that forms on the component side of the solder joint.

Key words: Electroplating, Innolot, Intermetallics, Lead-free Solders, LFPAK, Matte-Sn, Mechanical Cycling, SAC, Thermal Cycling.

INTRODUCTION

A fundamental understanding of the various factors affecting the reliability of Pb-free solder joints under cyclic thermal and mechanical loads is required for automotive applications. Electronic components such as LFPAK-MOSFETs (LFPAK) with gull-wing shaped pins are commonly used in automotive applications where the solder joints are subjected to both thermal and mechanical strains during service. The combined loading increases the sensitivity of the processing parameters to early fatigue failures. Several studies on solder joint reliability were performed under pure thermal or pure mechanical cyclic loading [1]–[4]. Only few studies have been conducted where both thermal and mechanical loading were simultaneously applied [5]–[7]. This study analyzes the impact of electroplating parameters of matte-Sn terminal finish on the thermo-mechanical reliability of LFPAK solder joints.

EXPERIMENTAL

In this study, the Cu lead-frames of the LFPAK components were coated with a Ni-underlayer (1-3 µm) to eliminate the effect of alloying elements in the Cu lead-frames on the type and growth of the intermetallic (IMC) phase that grows on the interface. The LFPAK lead-frames were then subjected to matte-Sn electroplating process according to the parameters provided in table 1.

Table 1: Matte-Sn electroplating parameters for LFPAK lead-frames with Ni underlayer.

Matte-Sn plating variant	Temperature (°C)	Current Density (A/dm²)	Organic Conc. (mL/L)
N	22	15	2
V3	17.5	20	2
V9	17.5	20	10
V27	27.8	20	10

The plating variant N represents the nominal electroplating parameters used under standard industrial conditions and V3, V9, V27 represent parameters at the tolerance limits in the electroplating process. The time of electroplating process was adjusted to obtain a matte-Sn coating of 10 µm. The matte-Sn thickness after electroplating was measured between 7-15µm in optical microscopy. The lead-frames were then bent and trimmed to obtain the LFPAK gull wing shape.

The LFPAK components were populated in 16 columns onto PCB test boards and reflow soldered using SAC305 or Innolot (Ag: 3.6, Cu: 0.6, Ni: 0.1, Sb: 1.3, Bi: 2.8 and remaining Sn) solder alloys. The reflow was done under similar conditions for both solder alloys with a ramp-soak-peak profile with maximum temperature of 260°C and time above liquidus (TAL) of 90s. The soldered PCB boards were placed with the top and bottom edges fixed

inside a bending vehicle consisting of a programmable electrical drive that imparts specified bending strains to the middle of the PCB boards. The bending vehicle is situated inside a temperature-controlled chamber as shown in figure 1a. The populated boards were subjected to 3-point in-phase bending and thermal cycling between 125°C/-40°C for 1000 and 2000 cycles. The load was applied at the center of the PCB (maximum microstrain of 1000/-600 ppm) which allowed the solder joints to experience 8 different levels of strain amplitude for the same thermal profile depending on the distance from the center of the PCB. A schematic of the in-phase thermo-mechanical bending test is shown in figure 1b. The individual LFPAK components were placed 0° with respect to bending direction. No electrical measurement was done to eradicate the effect of electrical current on the solder joint. The details of the experimental procedure are explained in [6]. In this study, the eight microstrain levels were reduced to 4 microstrain sets as seen in table 2 due to the negligible difference in solder joint performance and to improve the statistical accuracy during analysis.

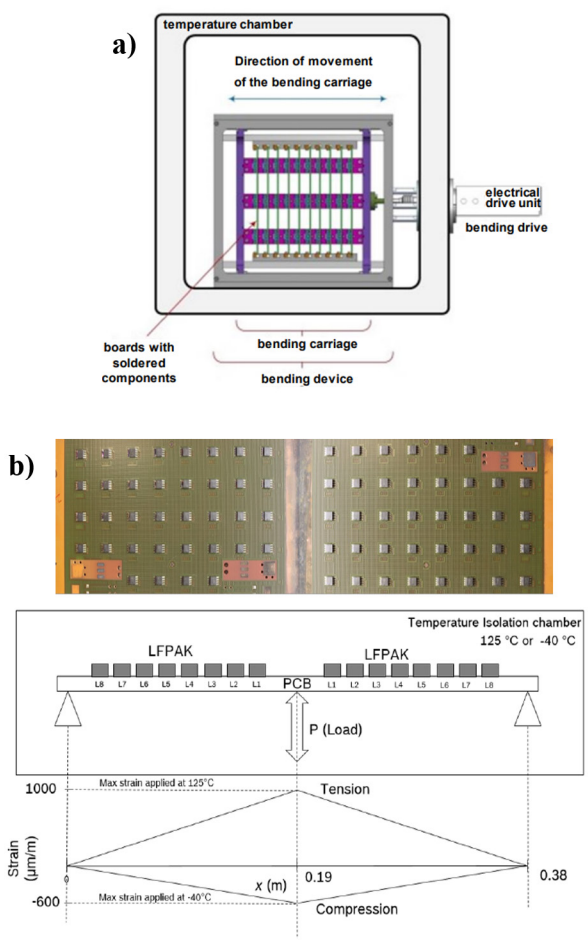

Figure 1: a) Schematic of the experimental bending vehicle used for in-phase thermo-mechanical bending test. b) Schematic showing the bending strain variation during tension and compression cycles.

After the specified number of cycles (1000 and 2000 cycles), the PCB boards with LFPAK components were taken out and subjected to metallographic processing and optical microscopy to obtain 2D cross sectional views of the solder joints. Figure 2a shows an example of a 2D cross section of a LFPAK solder joint after 2000 cycles. Figure 2b shows the schematic of LFPAK solder joint cross-section containing two cracks and the definitions of crack lengths and solder joint length. The total crack length (crack 1 length + crack 2 length + ….(if any)) present in the solder joint were divided by the solder joint length to obtain the crack %. To reduce the error in approximating 3D crack surface to a 2D cross-section plane, the crack % were measured for minimum 5 samples with same experimental conditions and the average crack % and standard deviations were calculated. Scanning electron microscopy (SEM) and energy dispersive X-ray spectroscopy (EDS) were done to investigate the microstructure and composition of the phases present at the interface.

Table 2: Tensile at 125°C and compressive at -40°C (indicated by - sign) microstrains (με) experienced by the LFPAK solder joints at eight microstrain levels (L1-L8). Eight microstrain levels were reduced to four microstrain sets and the corresponding average strain amplitude (ε_a) was calculated for each set.

με set	με levels	με applied at 125°C (ppm)	με applied at -40°C (ppm)	Strain amplitude εa= Δ(με)/2 (ppm)	Average εa per set (ppm)
1	L1	896.6	-541.2	718.9	678.3
	L2	793.1	-482.4	637.7	
2	L3	689.7	-423.5	556.6	516.0
	L4	586.2	-364.7	475.5	
3	L5	482.8	-305.9	394.3	353.8
	L6	379.3	-247.1	313.2	
4	L7	275.9	-188.2	232.0	191.5
	L8	172.4	-129.4	150.9	

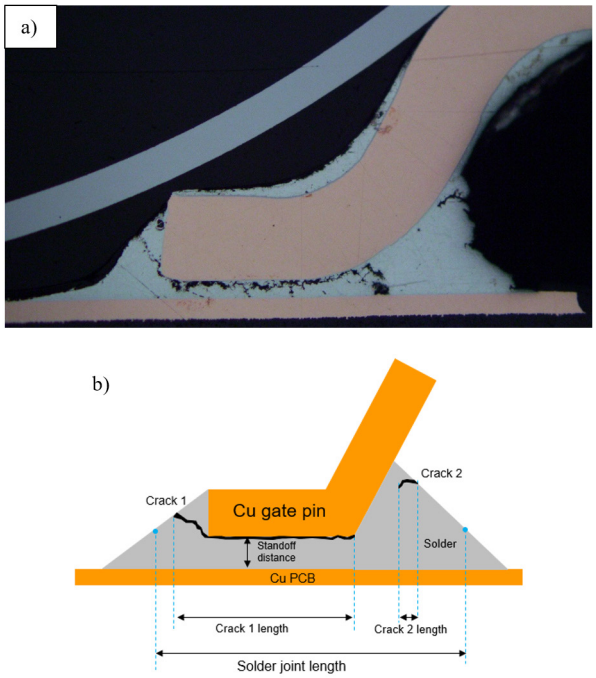

Figure 2: a) 2D cross sectional view of the LFPAK gull wing solder joint after 2000 cycles, b) Schematic of LFPAK cross-section containing two cracks showing the definitions of crack lengths and solder joint length.

RESULTS AND DISCUSSION

Statistical analysis of LFPAK solder joints after 1000 and 2000 thermo-mechanical fatigue cycles

After thermo-mechanical cycling for 1000 and 2000 cycles, the crack percentage values were calculated for the LFPAK solder joints. The crack percentage values were subjected to pareto analysis to find the significance of each factor used in this study: A) Strain amplitude , B) Solder alloy, C) Electroplating parameter and D) Number of fatigue cycles.

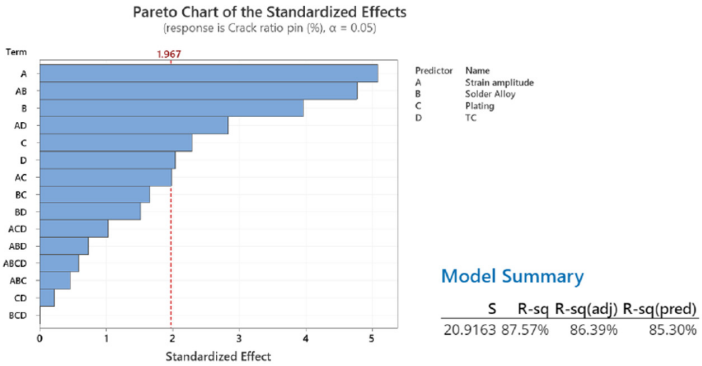

Figure 3: Pareto plot of crack percentage showing statistically significant main factors and interaction factors

The strain amplitude is taken as the continuous predictor and the order of significance of each factor and their interaction effects can be seen in figure 3. The Pareto chart uses a standardized effects chart calculated using t-statistic to help visualize relative significance of each factor and its interactions. A reference line which was calculated based on the chosen confidence interval (95%) helps distinguish the most significant factors. In terms of main effects, the applied microstrain (A) has the highest impact followed by type of solder alloy (B), matte-Sn electroplating parameter (C) and no. of fatigue cycles (D) respectively. With respect to interaction effects, the AB interaction effect is the most significant followed by AD and AC. Higher order parameters are not statistically significant and can be ignored. Goodness of mode l fit is shown by the higher values of both R-sq and R-sq(pred) values.

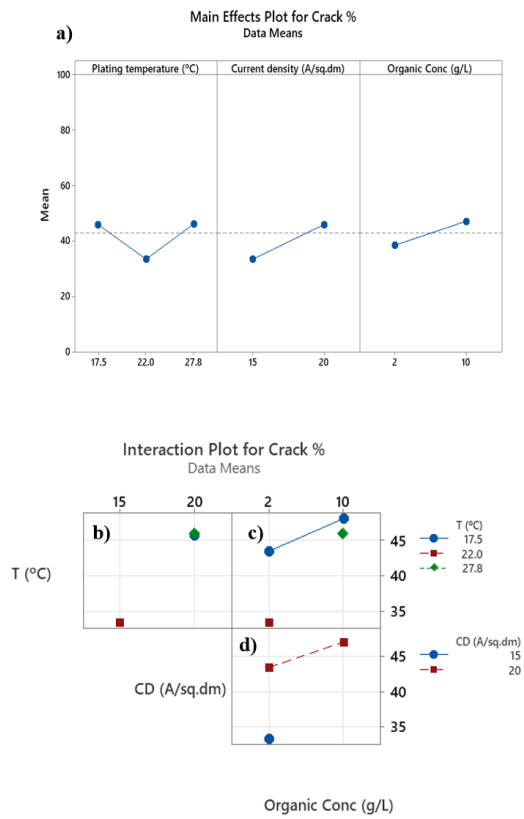

Figure 4: a) Main effects plot showing the influence of individual electroplating parameters on the mean crack percentage. b)-d) Interaction plot of crack% showing the interaction effects of the electroplating parameters: plating temperature (T), current density (CD) and organic concentration (g/L).

The main effects shown in figure 4a provides information on the influence of individual electroplating parameters on the mean crack percentage. Plating temperature does not have a direct relationship with obtained crack percentages. There is a narrow process window around 22°C with respect to plating temperature which can provide good thermo-mechanical performance. With respect to current density, there is an increase in mean crack percentage irrespective of other plating parameters. Higher current densities

can increase the impurity levels in the plating which decreases the thermo-mechanical performance. The organic concentration in the electrolyte during plating also has direct relationship to mean crack percentages. But the influence of individual factors is not straightforward as combinations of these factors results in varied performance. Figure 4b-4d shows the interaction plot which captures the interaction between various electroplating parameters. Figure 4b shows the dependence of crack percentage on plating temperature (T) and current density (CD) at constant organic concentration in the electrolyte. As the current density increases to 20 A/dm^2, average crack percentage is increased by almost same magnitude irrespective of whether the plating temperature was lowered to 17.5°C or increased to 27.8°C. In figure 4c, the effect of increasing the organic concentration is shown at various temperatures. At the organic concentration level of 2g/L (N and V3), the average crack percentage increased by a large magnitude as the temperature decreased from 22°C to 17.5°C. At the organic concentration level of 10g/L (V9 and V27), the mean crack percentage is lowered as the temperature increased from 17.5°C to 27.8°C. Figure 4d depicts that the mean crack percentage increases as the organic concentration in the electrolyte increases at higher constant current density of 20 A/dm^2. Thus, increasing the organic content in the electrolyte decreases the thermo-mechanical performance irrespective of plating temperature and current density. Due to the interaction of all three plating parameters, it is pertinent to further discuss the results of the thermo-mechanical test in terms of the plating variants (N, V3, V9, V27) instead of individual plating parameters.

The mean crack percentage of each plating variant is plotted as a function of strain amplitude for SAC305 and Innolot (IL) solder alloys after 1000 and 2000 cycles in figure 5. The error bar originates from the nature of cross section which shows just one plane of a 3D crack surface. Below a threshold strain amplitude of 250 ppm, the crack percentages obtained between the different plating conditions (N, V3, V9, V27) is negligible or close to zero for both SAC305 and Innolot solder joints. This implies that if the LFPAK components were tested with a pure temperature cycle test, the effects of plating parameters and/or type of solder alloy cannot be distinguished within the test limits of 2000 cycles. Therefore, the difference in the crack percentage obtained at an early stage (<2000 cycles) arises from the combination of thermal and applied strain contributions.

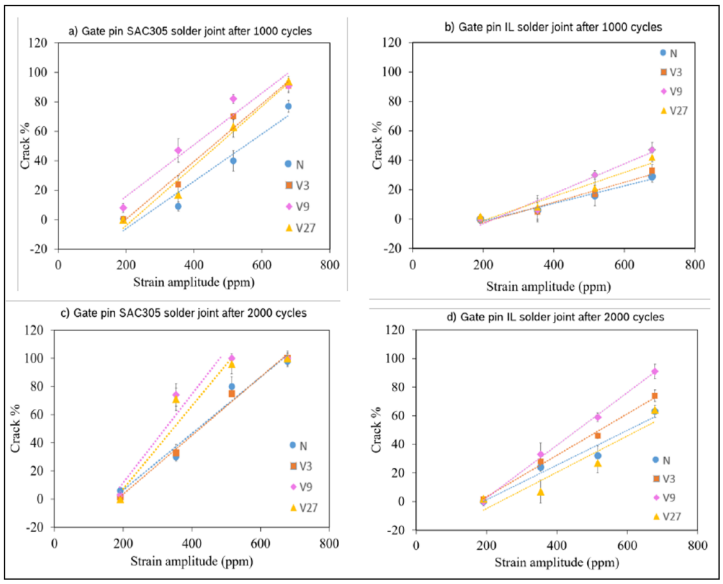

Figure 5: Strain amplitude vs crack percentage with various matte-Sn plating parameters: a) SAC305 soldered LFPAK after 1000 cycles, b) Innolot (IL) soldered LFPAK after 1000 cycles, c) SAC305 soldered LFPAK after 2000 cycles, d) Innolot soldered LFPAK after 2000 cycles. Note here that the crack percentage values are physically bound between 0% and 100%.

Comparing the solder alloy performance, the Innolot solder joints show very low crack percentage values than SAC305 solder joints after both 1000 and 2000 cycles for the same strain amplitude. The Innolot solder joints did not fail to 100% even at the maximum applied strain after 1000 cycles whereas the SAC solder joints started showing complete failure at the maximum applied strain after 1000 cycles. After 2000 cycles, 100% crack propagation occurred in Innolot solder joints which experienced the maximum strain amplitude. In comparison, the SAC solder joints showed complete failure at 516 ppm strain amplitude. The difference in reliability performance between SAC and Innolot solder joints pertains to the higher creep resistance of the Innolot solder alloy compared to the SAC305 solder alloy because of the combined effect of solid solution strengthening and enhanced precipitation hardening with large concentration of IMC precipitates in the solder matrix [8].

Considering the plating variants, the LFPAK solder joints plated with parameter N showed the lowest crack percentage whereas the solder joints with parameter V9 showed the highest crack percentage values for both SAC305 and Innolot after 1000 cycles. After 2000 cycles, all the plating variants in SAC solder joints showed 100% crack propagation at 516 ppm and 678.3 ppm strain amplitudes. At 353 ppm, V9 and V27 (plated with higher organic concentration) in the electrolyte have 80% mean crack percentage at 353 ppm whereas N and V3 (plated with lower organic concentration) have 40% mean crack percentage. In the case of Innolot solder joints after 2000 cycles, V9 solder joints exhibited the higher crack percentages at all strain amplitudes and was the only plating variant which exhibited 100% crack. All the other plating variants (V3, V27, N) performed in a similar way at their respective strain

amplitude levels. V9 contains larger amount of organic additives in the electrolyte during matte-Sn electroplating process and the plating was done at lower temperature (17 °C) compared to nominal temperature (22°C) . The higher concentration of organic additives is added to reduce the grain size of deposited Sn but the organic additives contaminate the Sn deposit at the grain boundaries [9]. Even though V27 contained higher organic additives during plating, the higher temperature could have assisted in the desorption of the organic molecules which resulted overall lower organic content in the plating. From these results, the combination of high organic additives in the electrolyte and lower temperature shows the worst reliability performance in both SAC305 and Innolot solder joints.

SEM and EDS investigation

Different regions of the gull wing developed IMC phases with different compositions (figure 6a) depending on their distance from the Cu-PCB pad irrespective of the solder alloy (SAC305 or Innolot) and the plating variant (V3, V9, V27, N). The top surface of the gull wing shows the diffusion of the Ni underlayer to form Ni-Sn IMC phase as seen in the Ni-map in figure 6b. EDS point scan revealed the composition of the Ni to be 40±0.3 at.% and that of Sn to be 59±0.4 at.% which corresponds to the Ni_3Sn_4 IMC phase. Here, the diffusion of Ni can be seen which acted as diffusion barrier for Cu (refer Cu map in figure 6b). The presence of Ag-Sn IMC precipitates from the solder alloy is also seen by the Ag map in figure 6b. On contrary, the bottom surface of the gull wing showed limited diffusion of Ni underlayer as seen in the Ni map in figure 6c which led to the formation of $(Cu,Ni)_6Sn_5$ IMC phase as seen by the Cu and Sn map in figure 6c. The line scan reveals the presence of Ni-gradient within the $(Cu,Ni)_6Sn_5$ phase. Usually, the expected phase to form between Ni and Sn at solder joint relevant temperatures (<300°C) is Ni_3Sn_4 as seen on the top surface of the pin [10], [11]. The formation of $(Cu,Ni)_6Sn_5$ IMC on a Ni surface on the bottom surface of the gull wing is due to the presence of excess Cu that diffused from the Cu surface on PCB side during reflow soldering and subsequently during thermo-mechanical cycling [12], [13]. Thermodynamically, the growth of $(Cu,Ni)_6Sn_5$ is possible when the Cu content in the Sn exceeds 8 at% locally [12]. But the SAC305/Innolot solder alloy contains maximum of 0.5 at% Cu. Hence the excess Cu must come from the Cu on the PCB side. Moreover, the microstructure changes from $(Cu,Ni)_6Sn_5$ to $(Cu,Ni)_6Sn_5$ + Ni_3Sn_4 to Ni_3Sn_4 along the bottom surface of the gull wing as the distance increases from the Cu on the PCB side as shown in figure 6a. The local IMC composition depends on the Cu concentration close to the interface between Ni underlayer and Sn. This fits perfectly to the argument that Cu on the PCB side acts as the Cu reservoir leading to change in IMC composition. On the Cu-PCB side, two IMC phases, Cu_6Sn_5 and Cu_3Sn IMC phases are formed which can be seen from the Cu-map in figure 6d. The thickness of the Cu_3Sn layer is thin in the standoff region (yellow box) compared to the region far from standoff due to the diffusion of Ni from the component side Ni from the Ni-underlayer must have dissolved into the Sn solder during reflow soldering and segregated towards the PCB pad side leading to enhanced growth rate of Cu_6Sn_5 phase and decreased the Cu_3Sn growth rate [14].

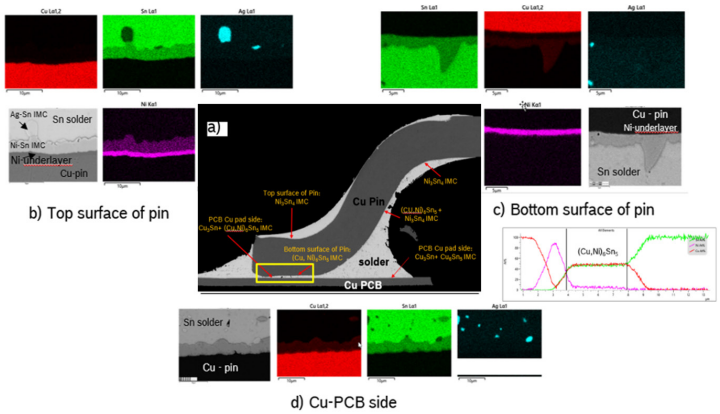

Figure 6: Elemental EDS mapping of Cu, Ni, Sn and Ag in V9-SAC gull wing pin solder joint after 2000 thermo-mechanical cycles. a) LFPAK gull wing with different IMC phases present in different regions, b) Top surface of the gull wing pin showing Ni_3Sn_4 phase c) Bottom surface of the gull wing pin showing $(Cu,Ni)_6Sn_5$ phase with Ni-gradient as seen by the line scan and d) Cu PCB side showing growth of Cu_6Sn_5 + Cu_3Sn phases. Yellow boxed region is the critical standoff region.

Even though crack initiations/shorter cracks have been observed from both meniscus sides (as seen in figure 2a) in components that have been subjected to lower strain levels, the crack reaches the IMC|Sn interface at the component side (yellow box zone) faster on the left meniscus due to the limited solder availability and further crack propagation characteristics are dependent on the $(Cu,Ni)_6Sn_5$ |Sn interface on the component side as shown in figure 7. Table 3 provide the thickness, roughness and Ni content of the $(Cu,Ni)_6Sn_5$ IMC measured on component side. The almost flat $(Cu,Ni)_6Sn_5$ IMC morphology of V9 which has lower Ni content (3 at%) in the $(Cu,Ni)_6Sn_5$ IMC enables the crack to propagate without any obstruction as seen in figure 7b whereas in case of N which has higher Ni (10 at%) in $(Cu,Ni)_6Sn_5$ IMC and has rougher morphology, the crack is deflected from the IMC/Sn interface towards the more ductile Sn as seen in figure 7a. The rougher interface increases the energy for crack propagation in comparison to a flatter IMC|Sn interface which attributes to lower crack percentages in solder joints which had N plating variant as opposed to the higher crack percentages in V9 for the same number of thermo-mechanical cycles. Thus, the electroplating parameters of matte-Sn influences the Ni-content and hence the morphology of the $(Cu,Ni)_6Sn_5$ IMC that forms on the Ni-underlayer on the component side. The standoff distances in this study were measured to have normal distribution (Avg: 22µm, standard deviation: ± 8µm) and no direct correlation were observed to the type of failure observed. The morphology of the $(Cu,Ni)_6Sn_5$ IMC in the standoff zone primarily determines the crack propagation characteristics for the standoff distances relevant in this study.

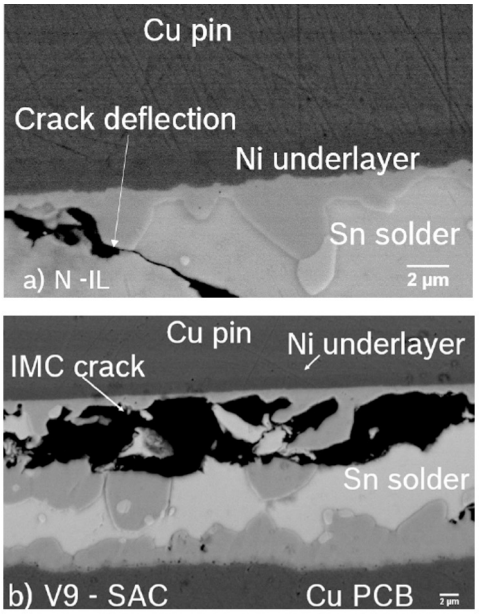

Figure 7: a) Crack deflected by the rough $(Cu,Ni)_6Sn_5$ IMC in N-Innolot solder joint. b) IMC crack propagated through the $(Cu,Ni)_6Sn_5$ IMC/solder interface in V9-SAC solder joint

Table 3: $(Cu,Ni)_6Sn_5$ IMC thickness and roughness in the standoff region for plating variant-solder combination after 2000 cycles. The gradient of Ni in IMC is provided by measuring the Ni at. % at the middle of the IMC and close to the IMC/solder interface using EDS area scans. The standard deviations are provided in brackets.

Plating Variant	Solder	IMC thick-ness (µm)	IMC rough-ness (µm)	Ni at. % middle of IMC	Ni at. % close to IMC/ solder	Ni at. % gra-dient
V3	SAC	3.43	1.73	7.5 (1.2)	2.3 (1.1)	5.2
V9	SAC	3.65	0.78	3.4 (0.9)	<0.5 (0.5)	2.9
V27	SAC	3.56	1.2	7.2 (1.1)	0.9 (0.3)	2.3
N	SAC	4.23	2.23	10.5 (0.9)	3.2 (0.9)	7.3
V3	IL	2.34	1.43	5.6 (0.8)	1.3 (0.6)	4.3
V9	IL	2.23	0.34	2.7 (1.6)	1.2 (0.8)	1.5
V27	IL	3.23	0.43	4.4 (0.8)	2.1 (0.6)	2.3
N	IL	3.34	1.92	8.4 (0.6)	3.4 (1.2)	5

CONCLUSIONS

The effect of matte-Sn electroplating parameters on the thermo-mechanical reliability has been studied and the following conclusions have been derived:

1. The combined effect of thermal and mechanical loads during thermo-mechanical cycling leads to early solder joint failure compared to pure thermal cycling. Minimum of 400 ppm of microstrain is required to visualize the effect of minor influencing factors such as matte-Sn electroplating parameters.

2. Regardless of the electroplating conditions, Innolot has high thermo-mechanical reliability than SAC305 solder alloy.

3. Electroplating parameters of matte-Sn have notable influence on the thermo-mechanical performance of both SAC and IL solder joints.

4. The electroplating parameters with high organic additives in the electrolyte and lower plating temperatures exhibits brittle failure through IMC crack mode.

5. Microstructural investigation suggests that the electroplating parameters affect the Ni content and morphology of the $(Cu,Ni)_6Sn_5$ IMC which inturn influences the crack propagation path either deflecting to Sn or continuing via IMC|Sn interface.

REFERENCES

[1] B. Vandevelde, M. Gonzalez, P. Limaye, P. Ratchev, and E. Beyne, "Thermal cycling reliability of SnAgCu and SnPb solder joints: A comparison for several IC-packages," Microelectronics Reliability, vol. 47, no. 2–3, pp. 259–265, Feb. 2007, doi: 10.1016/j.microrel.2006.09.034.

[2] C. Shen et al., "Packaging Reliability Effect of ENIG and ENEPIG Surface Finishes in Board Level Thermal Test under Long-Term Aging and Cycling," Materials, vol. 10, no. 5, p. 451, Apr. 2017, doi: 10.3390/ma10050451.

[3] P. Choudhury and S. Sarkar, "Development of lead-free alloys with ultra-high thermo- mechanical reliability," Proceedings of SMTA International, 2015.

[4] H. Li, T. An, X. Bie, G. Shi, and F. Qin, "Thermal fatigue reliability analysis of PBGA with Sn63Pb37 solder joints," in 2016 17th International Conference on Electronic Packaging Technology (ICEPT), Wuhan: IEEE, Aug. 2016, pp. 1104–1107. doi: 10.1109/ICEPT.2016.7583318.

[5] B. Torres-Montoya, D. Duffek, J. Mason, E. Corona, M. Chengalva, and M. Cavanaugh, "Effects of combined cyclic thermal and mechanical loading on fatigue of solder joints," in The Ninth Intersociety Conference on Thermal and Thermomechanical Phenomena in Electronic Systems (IEEE Cat. No.04CH37543), Las Vegas, NV, USA: IEEE, 2004, pp. 280–286. doi: 10.1109/ITHERM.2004.1318294.

[6] U. Welzel, L. Lagarde, Y. Wang, F. Schempp, and R. B. GmbH, "Temperature Cycling with Bending to Reproduce Typical Product Loads", Proceedings of SMTA International, 2020.

[7] I. Kim and S.-B. Lee, "Fatigue Life Evaluation of Lead-free Solder under Thermal and Mechanical Loads," in 2007 Proceedings 57th Electronic Components and Technology Conference, Sparks, NV, USA: IEEE, 2007, pp. 95–104. doi: 10.1109/ECTC.2007.373782.

[8] Q. B. Tao, L. Benabou, K. L. Tan, J. M. Morelle, and F. B. Ouezdou, "Creep behavior of Innolot solder alloy using small lap-shear specimens," th Electronics Packaging Technology Conference, p. 6, 2015.

[9] A. Sharma, S. Das, and K. Das, "Pulse Electroplating of Ultrafine Grained Tin Coating," in Electroplating of Nanostructures, M. Aliofkhazraei, Ed., InTech, 2015. doi: 10.5772/61255.

[10] C. Ghosh, "Study on important diffusion parameters of binary Ni_3Sn_4 phase," J Mater Sci: Mater Electron, vol. 24, no. 7, pp.

2558–2561, Jul. 2013, doi: 10.1007/s10854-013-1133-2.

[11] C. Wang and J. Liu, "Effects of Sn thickness on morphology and evolution of Ni_3Sn_4 grains formed between molten Sn and Ni substrate," Intermetallics, vol. 61, pp. 9–15, Jun. 2015, doi: 10.1016/j.intermet.2015.02.002.

[12] T. Laurila, V. Vuorinen, and J. K. Kivilahti, "Interfacial reactions between lead-free solders and common base materials," Materials Science and Engineering: R: Reports, vol. 49, no. 1–2, pp. 1–60, Mar. 2005, doi: 10.1016/j.mser.2005.03.001.

[13] A. Wierzbicka-Miernik, J. Wojewoda-Budka, K. Miernik, L. Litynska-Dobrzynska, and N. Schell, "Characteristics of intermetallic phases in Cu/(Sn,Ni) diffusion couples annealed at 220 °C," Journal of Alloys and Compounds, vol. 693, pp. 1102–1108, Feb. 2017, doi: 10.1016/j.jallcom.2016.09.147.

[14] V. A. Baheti, S. Kashyap, P. Kumar, K. Chattopadhyay, and A. Paul, "Solid–state diffusion–controlled growth of the intermediate phases from room temperature to an elevated temperature in the Cu–Sn and the Ni–Sn systems," Journal of Alloys and Compounds, vol. 727, pp. 832–840, Dec. 2017, doi: 10.1016/j.jallcom.2017.08.178.

Corporate Members

4Front Solutions

AA Technology Inc.

AAA Test Lab

Abatek Americas Inc

AbelConn, LLC

Accu-Assembly Inc.

Accu-Automation Corporation

Accurate Technologies, Inc.

ACDi

ACL STATICIDE

actnano Inc.

ADCO Circuits, Inc.

Advanced Component Testing

Aegis Software

AI Technology, Inc.

AIM Solder

Air Products and Chemicals Inc

Air-Vac Engineering

Akrometrix LLC

Alert Tech SMT

All Flex Solutions

Allfavor Technology

Alltemated

Alternative Manufacturing Inc.

Altronic, LLC (A Member of the Hoerbiger Group)

Amazon

American Hakko Products, Inc.

American Standard Circuits, Inc.

American Technology Components Inc.

Amitron Corporation

Amphenol Borisch Technologies

Analog Technologies Corporation

ANDA TECHNOLOGIES USA INC

Annapolis Micro Systems, Inc.

Ansen Corporation

Apollo Seiko

Applicad Inc.

Aqueous Technologies

Arbell Electronics Inc

ARCADIA TEST INC

Arc-Tronics, Inc.

Ascentec Engineering

ASM Assembly Systems

ASYS Group Americas Inc.

Aven, Inc.

Axiom Electronics LLC

BBM, Inc.

Benchmark Electronics, Inc

Berkshire Corp.

BEST Inc.

BGA Test & Technology

Bittele Electronics Inc.

BlueRing Stencils

BPM Microsystems

Brady Corporation

Braun Electronic Components

BSE INC

BTU International, Inc.

BTW Inc.

Burton Industries, Inc.

CalcuQuote

Carel USA Inc.

Celestica, Inc.

CEMSI

CheckSum LLC

Cimetrix Incorporated

Cirtronics

CO-AX Technology, Inc.

Cofactr Inc

Colonial Electronic Manufacturers Inc.

Comet X-Ray

Comtree Inc.

Conductive Containers

Conecsus Metals Conecsus LLC

Continental

Creation Technologies Inc.

Creative Electron, Inc.

Critical Manufacturing

CRM Synergies

Crown Equipment Corporation

Cruise LLC

Crystal Mark, Inc.

CSE

CTI Systems

Cumberland Electronics Strategic Supply Solutions CE3S

Cypress Technologies LP

Daktronics, Inc.

Datest Corporation

Datum Alloys

DELO Industrie Klebstoffe GmbH & Co. KGaA

DG Marketing Corporation

Digital Audio Labs

Divelbiss Corporation

Dorigo Systems Ltd.

Ducommun Incorporated

Dymax Corporation

East West Wisconsin

EI Microcircuits

EIS

ELANTAS PDG, Inc.

Electronic Interconnect

Electronic Systems, Inc.

Electronic Technologies International

Element Materials Technology Baltimore

Ellsworth Adhesives

Eltek USA Inc.

Enercon

Engent, Inc.

EPTAC LLC

ESSEMTEC USA

Europlacer Americas

Express Manufacturing Inc.

Extant Aerospace

Facebook

Fancort Industries, Inc

FCT Assembly, Inc.

Finetech

Flex Mexico

Flex USA

FlexLink Systems, Inc.

FTG Circuits Haverhill

Fuji America Corporation

Fusion EMS

GÖPEL electronic GmbH

Garland Service Company

Garmin International

GEN3 System

Glenbrook Technologies Inc.

Global Shop Solutions

GLOBAL SOLUTIONS ELECTRONICS

Google

Great Lakes Engineering

Hanwha Techwin Automation Americas. Inc.

Harman de Mexico S de RL de CV

Heller Industries

Hentec Industries / RPS Inc.

HISCOMEX

Honeywell FM&T

HONG KONG LUK ELECTRONICS CO., LIMITED

Horizon Sales

Hughes Circuits, Inc.

HumiSeal Europe Ltd.

HZO

I Source Technical Services, Inc.

iBtest

ICAPE USA

IDENTCO

IKEUCHI USA, INC.

IMAT, Inc

InCap Electronics US

Indium Corporation

Ingenieria y Control Integral

INGUN USA, Inc.

Innovative Circuits, Inc.

Inovaxe Corporation

Integrated Circuit Works

Intel Corporation

INTERFLUX

Interlatin S. de R.L. de C.V

Intervala, LLC.

Intraratio Corporation

INVENTEC Performance Chemicals

IPS Assembly Corporation

IPTE, LLC

iST-Integrated Service Technology Inc.

ITEC LATIN AMERICA

ITW Contamination Control

ITW EAE

Jabil Circuit, Inc. (JDAS-STP)

JAK ELECTRONICS LIMITED

Japan Unix

JBC Tools USA Inc.

JH Technologies

John Deere Electronic Solutions, Inc.

Juki Automation Systems

Juniper Networks

KATEK Group

Keysight Technologies

KIC

Kimball Electronics Inc.

Koh Young Technology Inc.

Koki Solder America Inc.

kolb Cleaning Technology GmbH

Kostal Ireland GMBH

KURTZ ERSA S.A. DE C.V.

Kurtz Ersa, Inc.

Kyowa Americas Inc.

KYZEN Corporation

L3HARRIS

LACROIX

LeeMAH Electronics, Inc.

Lexicon Technologies Inc

Libra Industries, LLC

Lockheed Martin

MacDermid Alpha Electronics Solutions

Mack Technologies Inc.

Magnalytix

Maquiladora de Servicios MMS Sa de CV

MaRC Technologies

Marco System Analysis and Development GmbH

Master Bond Inc.

Matric LTD

MBDA (UK)

MEK Americas

MELECS Electronics Queretaro

Metallic Resources, Inc.

Metcal OK International

MexSer

MG Chemicals

Microboard

MicroCare Corporation

Microchip

Micron Corporation

MicroScreen, LLC

Microtech Laboratories LLC

Mid America Taping and Reeling, Inc.

Millennium Circuits Limited

Miller Electric Mfg. Co. - Components Division

Milwaukee Electronics

Milwaukee Tool

Mirac, LLC.

Miraco, Incorporated

Mirtec Corporation

MOMENTIVE PERFORMANCE MATERIAL

MTE Solutions, Inc.

Murray Percival Company

Mycronic, Inc

N.F. Smith & Associates, L.P.

NAS Electronics

National Instruments

NCAB Group USA

Newtechnik Ind.Com.Prod.Eletr.ltda

Nihon Superior Company, Ltd.

Nikon Metrology, Inc.

Nokia Bell Labs

Nordson Test & Inspection

NPI Services, Inc.

NPI Technologies, Inc.

nScrypt

NSW Automation Sdn. Bhd.

NVIDIA Corporation

OES Inc.

OmniOn Power

Omron Inspection Systems

PAC Global, Inc.

PAC Mexico

PACE Worldwide

PalPilot International Corporation

Panasonic

PARMI USA INC.

Partstack Corporation

PCB Connect Inc.

PCEA

PDR Americas

PEMTRON CORPORATION

Performance Review Institute

Performance Technologies Group, Inc.

PFC Flexible Circuits

Pillarhouse USA, Inc.

Pinnacle Technology Group

Plato Systems

Plexus Corp.

Polyonics, Inc.

Powell Industries, Inc.

PowerArena

Powertrain Control Solutions

PPSI

Practical Components

Precision PCB Services, Inc.

Price Electronics

PRIDE Industries

Prime Technological Services

Printed Circuits Corp.

Pro-Active Engineering LLC

ProActive Process Solutions Group, LLC ~ Manufacturers' Representatives

Process Sciences, Inc.

Production Automation Corporation

Projects Unlimited, Inc.

PROMATION USA

Promex Industries, Inc.

PVA

PVA TePla OKOS

Quiptech

Raven Industries Inc.

Rawinski GmbH

RBB Systems

Renishaw PLC

Repstronics

Resources Unlimited Co. USA

Restronics

Retronix

Rich Sales

Rochester Institute of Technology (RIT)

ROCKA Solutions

Rockwell Automation

Saki America Inc.

Samtec

Saturn Electronics Corporation

ScanCAD International, Inc.

SCHUNK Electronic Solutions

Schweitzer Engineering Labs

Scienscope

Securitas Healthcare

SEHO North America, Inc.

Seica Inc.

Seika Machinery, Inc.

Senju Comtek Corporation

SHENMAO Technology, Inc.

Shenzhen HTGD Intelligent Equipment Co., Ltd

Shenzhen KHJ Technology Co.,Ltd

Shin-Etsu Silicones of America

Siborg Systems Inc

SICK, Inc.

Signum, LLC

Simco-Ion Technology Group

SLB

SMART Microsystems

Smart Splice, LLC

SMarTsol Technologies

SMT America

SMT Resource Equipment

SMT SOLID

SMT Union

SMTo Engineering

SMTVYS LLC

SMTXTRA USA INC

SolderStar LLC

Southwest Research Institute

Space Dynamics Laboratory

Spartronics

Sparx Engineering

SPEA America

Specialized Coating Services

Specialty Coating Systems, Inc.

Spectrum AMT

StaticStop a division of SelecTech, Inc.

StenTech, Inc.

STI Electronics, Inc.

STIM Canada Inc.

Sunshine Global Circuits

SVTronics, Inc.

Synapse Electronique Inc.

Syncro Corp

SynQor Inc

Sypris Electronics, LLC

Tamura

Technica, USA

Technimark, Inc.

Techtron Systems Inc.

Teknek

Teradyne, Inc.

Test Research, Inc.

Test Technology Associates

TESTEQUITY

Texmac/Takaya, Inc.

The Jefferson Project

The Test Connection, Inc.

Thermaltronics USA, Inc.

Tintronics

TouchPad Electronics LLC

Trans Tec America

Transforming Technologies

Trenton Technology Inc.

TT Electronics

Unison Industries

Universal Instruments

Universal Scientific Industrial Co. Ltd.

Univertools

USM Reps

Valtronic Technologies (USA) Inc.

Variosystems, Inc.

VCcount by Visiconsult X-ray Systems & Solutions GmbH

Venkel Ltd.

Versa Electronics

VEXOS

Virtual Industries Inc.

Viscom

Vision Engineering

Vitrox Technologies Sdn. Bhd.

VJ Electronix, Inc.

VSE

Watchfire Signs

Weller

Western Digital

West-Tech Materials, Inc.

WIN SOURCE ELECTRONICS

WinTronics, Inc.

WORLD Electronics

XDry Corporation

X-Treme Series Auto Dry Cabinets

Yield Engineering Systems

Zapp Precision Strip

Zentech Manufacturing, Inc.

ZESTRON Corporation

Zollner Electronics Inc.

Zymet, Inc.

6600 City West Parkway, Suite 300
Eden Prairie, MN 55344 USA

Phone: +1-952-920-7682
Fax: +1-952-926-1819

E-Mail: smta@smta.org
Web site: www.smta.org